

Banner appropriate to article type will appear here in typeset article

# Turbulent diffusion-cascade interaction

**E. Fuentes Noriega<sup>1</sup> and J.C. Vassilicos<sup>1†</sup>**

<sup>1</sup>Univ. Lille, CNRS, ONERA, Arts et Metiers Institute of Technology, Centrale Lille, UMR 9014, LMFL - Laboratoire de Mécanique des Fluides de Lille, Kampé de Fériet, F-59000 Lille, France

(Received xx; revised xx; accepted xx)

In the decay region around the centreline of three qualitatively different turbulent plane wakes, the turbulence is non-homogeneous and two-point turbulent diffusion counteracts the turbulence cascade all the way down to scales smaller than the Taylor length. It is found that the sum of the inter-space transfer rate and the horizontal part of the inter-scale transfer rate of horizontal two-point turbulent kinetic energy is approximately proportional to the turbulence dissipation rate in the inertial range with a constant of proportionality between  $-0.6$  and  $-1$  depending on wake and location within the wake, except at the near-field edge of the decay region.

**Key words:** wakes, turbulence theory

---

## 1. Introduction

Inter-scale turbulence transfers and the turbulence cascade are pivotal in turbulent flows. In statistically stationary homogeneous turbulence, the average inter-scale transfer rate balances the turbulence dissipation rate over an inertial range of length scales which widens as the Reynolds number increases. This scale-by-scale equilibrium is a prediction of the Kolmogorov theory which is specifically designed for statistically stationary homogeneous turbulence (see Frisch 1995). However, turbulent flows are typically non-homogeneous and inter-space turbulence transfers (two-point turbulent diffusion) do not necessarily average to zero. In this case they contribute to the average scale-by-scale turbulent kinetic energy budget and must therefore be taken into account. In fact, concurrent inter-scale and inter-space transfers were identified by Marati *et al.* (2004) more than twenty years ago in direct numerical simulations of fully developed turbulent channel flow. Cimarelli *et al.* (2013, 2016, 2021, 2024) studied how turbulent energy evolves through both physical and scale spaces and identified paths for this evolution in both wall-bounded turbulent flows and planar jets. Direct effects of spatial non-homogeneity and coherent structures on inter-scale transfer rates were also reported in spatially evolving wakes (see Thiesset & Danaila 2020). Even in statistically homogeneous turbulence where inter-space transfer rates average to zero at all length-scales, one cannot fully describe inter-scale transfer rate fluctuations without taking inter-space transfer rates into account. Indeed, the fluctuations of the solenoidal part of the inter-space transfer rates have recently been shown to be anti-correlated with the fluctuations of the

† Email address for correspondence: john-christos.vassilicos@cnrs.fr

solenoidal part of the inter-scale turbulence transfer rates (Larsen & Vassilicos 2023). Are there such clear simple relations between parts of average inter-scale turbulence transfers and average inter-space turbulence transfers in statistically non-homogeneous turbulence? How do these average transfer rates depend on two-point separation and how do they compare with the turbulence dissipation rate? Is it necessary that there should be a tendency towards local homogeneity at small enough inertial length scales as commonly believed?

We answer these questions for three turbulent wakes of two side-by-side parallel identical square prisms by analysing Two-Dimensional Two-Component Particle Image Velocimetry (2D2C PIV) data obtained by Chen *et al.* (2021). These three planar turbulent wakes are qualitatively different, thereby allowing us to test the generality of our results. We concentrate attention on the decaying wake, i.e. the region around the centreline which is far enough from the square prisms for the local Reynolds number to decay with streamwise distance.

Given that the 2D2C PIV data at our disposal provide information about the turbulent fluctuating velocities  $u'_1$  and  $u'_2$  in the streamwise and cross-stream directions only, both of which are in the horizontal plane normal to the spanwise direction of the vertical prisms, this paper's focus is on the inter-scale transfer of horizontal turbulent kinetic energy.

In the following section we present the paper's theoretical framework. In section 3 we describe the 2D2C PIV data of Chen *et al.* (2021) and in section 4 we present our analysis of these data with particular focus on the two-point turbulent kinetic energy transfer processes. Conclusions are drawn in section 5 where we highlight some key open questions regarding the intimate link between the dissipation rate, the cascade and the turbulent diffusion in non-homogeneous situations.

## 2. Two-point horizontal turbulent kinetic energy budget

We are interested in the budget of the horizontal two-point turbulent kinetic energy, which is defined as  $\delta K_h \equiv \frac{1}{2}[(\delta u'_1)^2 + (\delta u'_2)^2]$  where  $\delta u'_i \equiv \frac{1}{2}[u'_i(\mathbf{X} + \mathbf{r}, t) - u'_i(\mathbf{X} - \mathbf{r}, t)]$  (for  $i = 1, 2, 3$ ) is a half-difference (high-pass filtered) fluctuating velocity component (Germano 2012). Given the horizontal 2D nature of the data used in this paper, we limit ourselves to horizontal separation vectors  $\mathbf{r} = (r_1, r_2, 0)$ . We consider statistically stationary turbulent velocity fields so that the budget is averaged over time and is for  $\overline{\delta K_h} \equiv \frac{1}{2}(\overline{\delta u'_1})^2 + (\overline{\delta u'_2})^2$  where the overbar signifies time-averaging. This two-point average energy defines the following scale-by-scale decompositions of the one-point horizontal energy  $K_h(\mathbf{X}) = |\frac{1}{2}\mathbf{u}'_h|^2$  (with  $\mathbf{u}'_h \equiv (u'_1, u'_2, 0)$ ) for  $i = 1$  and  $i = 2$ :

$$\int_0^{L_{i0}} \frac{d}{dr_i} \overline{\delta K_h} dr_i = \overline{K_h(\mathbf{X} + \mathbf{R}_i)} + \overline{K_h(\mathbf{X} - \mathbf{R}_i)} \quad (2.1)$$

where  $\mathbf{R}_1 = (L_{10}, 0, 0)$  and  $\mathbf{R}_2 = (0, L_{20}, 0)$  are the separation vectors with the smallest separations  $L_{i0}$  for which the two-point correlations  $\overline{\mathbf{u}'_h(\mathbf{X} + \mathbf{R}_i) \cdot \mathbf{u}'_h(\mathbf{X} - \mathbf{R}_i)}$  vanish. These separations  $L_{10}$  and  $L_{20}$  can be thought of as characteristic streamwise and cross-stream sizes of the largest “eddy” centered at  $\mathbf{X}$ , and  $\frac{d}{dr_i} \overline{\delta K_h}$  are energy densities per unit separation distance for each  $i = 1, 2$ . These energy densities decompose the sum of the horizontal turbulent kinetic energies at  $\mathbf{X} + \mathbf{R}_i$  and  $\mathbf{X} - \mathbf{R}_i$ . Of course, these decompositions can be generalised to any other quantity (e.g. the full turbulent kinetic energy) and makes sense only when finite separations  $L_{i0}$  exist; we checked that this is indeed the case for all the data used here.

For the budget of  $\delta K_h$  we also need to define the half-sum (low-pass filtered) fluctuating velocity vector  $\mathbf{u}'_{\mathbf{X}} \equiv \frac{1}{2}[\mathbf{u}'(\mathbf{X} + \mathbf{r}, t) + \mathbf{u}'(\mathbf{X} - \mathbf{r}, t)]$  (Germano 2012) and the half-difference fluctuating pressure  $\delta p' \equiv \frac{1}{2\rho}[\overline{p'(\mathbf{X} + \mathbf{r}, t)} - \overline{p'(\mathbf{X} - \mathbf{r}, t)}]$  (in terms of the fluid density  $\rho$  and

the fluctuating pressure  $p'$ ) as well as the half-sum and half-difference mean velocity fields  $\bar{\mathbf{u}}_{\mathbf{X}} \equiv \frac{1}{2}[\bar{\mathbf{u}}(\mathbf{X} + \mathbf{r}) + \bar{\mathbf{u}}(\mathbf{X} - \mathbf{r}, t)]$  and  $\delta\bar{\mathbf{u}} \equiv \frac{1}{2}[\bar{\mathbf{u}}(\mathbf{X} + \mathbf{r}) - \bar{\mathbf{u}}(\mathbf{X} - \mathbf{r})]$  in terms of the mean flow field  $\bar{\mathbf{u}}$ . At any position  $\mathbf{X}$  in physical space and for any two-point separation vector  $2\mathbf{r}$  this budget can be written as (see Hill 2001, 2002; Chen & Vassilicos 2022; Beaumard *et al.* 2024)

$$L_T - P + T_X + \Pi_h = T_p + D - \tilde{\varepsilon}_1 - \tilde{\varepsilon}_2, \quad (2.2)$$

where the linear transport rate  $L_T$ , the two-point turbulence production rate  $P$ , the inter-space transport rate  $T_X$ , the inter-scale transfer rate  $\Pi_h$ , the two-point pressure-velocity term  $T_p$  and the viscous diffusion rate  $D$  are defined below.

$$L_T \equiv \bar{\mathbf{u}}_{\mathbf{X}} \cdot \nabla_{\mathbf{X}} \overline{\delta K_h} + \delta\bar{\mathbf{u}} \cdot \nabla_{\mathbf{r}} \overline{\delta K_h}, \quad (2.3)$$

where  $\nabla_{\mathbf{X}}$  and  $\nabla_{\mathbf{r}}$  are the gradients with respect to  $\mathbf{X}$  and  $\mathbf{r}$  respectively. This term represents transport of two-point turbulent kinetic energy by the mean flow and is therefore referred to as linear to distinguish it from the non-linear terms  $T_X$  and  $\Pi_h$  which represent transport of two-point turbulent kinetic energy by fluctuating turbulent velocities.

$$P \equiv -\overline{\delta u'_1 \mathbf{u}'_{\mathbf{X}}} \cdot \nabla_{\mathbf{X}} \overline{\delta u_1} - \overline{\delta u'_2 \mathbf{u}'_{\mathbf{X}}} \cdot \nabla_{\mathbf{X}} \overline{\delta u_2} - \overline{\delta u'_1 \delta \mathbf{u}'} \cdot \nabla_{\mathbf{r}} \overline{\delta u_1} - \overline{\delta u'_2 \delta \mathbf{u}'} \cdot \nabla_{\mathbf{r}} \overline{\delta u_2}, \quad (2.4)$$

$$T_X \equiv \nabla_{\mathbf{X}} \cdot \overline{\mathbf{u}'_{\mathbf{X}} \delta K_h}, \quad (2.5)$$

$$\Pi_h \equiv \nabla_{\mathbf{r}} \cdot \overline{\delta \mathbf{u}' \delta K_h}, \quad (2.6)$$

$$T_p \equiv -\overline{\delta u'_1 \frac{\partial}{\partial X_1} \delta p'} - \overline{\delta u'_2 \frac{\partial}{\partial X_2} \delta p'}, \quad (2.7)$$

where  $X_1$  and  $X_2$  are the horizontal streamwise and cross-stream coordinates of  $\mathbf{X}$  and

$$D \equiv \frac{\nu}{2}(\nabla_{\mathbf{X}}^2 + \nabla_{\mathbf{r}}^2)\overline{\delta K_h}, \quad (2.8)$$

where  $\nu$  is the fluid's kinematic viscosity. The two-point turbulence dissipation rates  $\tilde{\varepsilon}_1$  and  $\tilde{\varepsilon}_2$  in (2.2) are defined as  $\tilde{\varepsilon}_i \equiv \frac{1}{2}(\varepsilon_i(\mathbf{X} + \mathbf{r}) + \varepsilon_i(\mathbf{X} - \mathbf{r}))$  where  $\varepsilon_i(\mathbf{X}) \equiv \nu(\partial u'_i / \partial x_j)^2$  with a sum over  $j = 1, 2, 3$  for any  $i = 1, 2$ . This definition also holds for  $i = 3$ .

If the turbulence is statistically homogeneous this budget reduces to

$$\Pi_h = T_p + D - \varepsilon_1 - \varepsilon_2, \quad (2.9)$$

which means that the inter-scale transfer rate  $\Pi_h$  of horizontal two-point turbulent kinetic energy is balanced by the pressure-redistribution rate  $T_p$  between  $\overline{\delta K_h}$  and  $\frac{1}{2}\overline{(\delta u'_3)^2}$ , the rate of molecular diffusion of  $\overline{\delta K_h}$  which is known to be negligible at scales larger than the Taylor length  $\lambda$  (see Laizet *et al.* 2013; Valente & Vassilicos 2015) and the dissipation rate of  $\overline{\delta K_h}$ . At scales larger than the Taylor length where we can neglect molecular diffusion, the inter-scale transfer rate  $\Pi_3$  of the vertical/spanwise two-point turbulent kinetic energy  $\frac{1}{2}\overline{(\delta u'_3)^2}$  obeys  $\Pi_3 \approx -T_p - \varepsilon_3$  in statistically stationary homogeneous turbulence so that the total inter-scale transfer rate  $\Pi_h + \Pi_3$  of the entire two-point turbulent kinetic energy balances the total turbulence dissipation rate, i.e.  $\Pi_h + \Pi_3 \approx -\varepsilon$  (where  $\varepsilon = \varepsilon_1 + \varepsilon_2 + \varepsilon_3$ ). This is the scale-by-scale Kolmogorov equilibrium which is a prediction specifically designed for statistically stationary and homogeneous turbulence (see Kolmogorov 1941; Frisch 1995).

The situation is different if the statistically stationary turbulent flow is not statistically homogeneous, in which case at least one of the three terms  $L_T$ ,  $P$  and  $T_X$  on the left hand side of equation (2.2) is not negligible. In this paper, we study the budget equation (2.2) in three qualitatively different turbulent wakes of two parallel square prisms placed normal to an incoming uniform flow. These flows are non-homogeneous in the plane normal to the square prisms but homogeneous and symmetric in the prisms' spanwise direction, thereby allowing the three terms  $L_T$ ,  $P$  and  $T_X$  to be fully evaluated from velocity data obtained by 2D2C PIV in the plane normal to the spanwise direction. The Taylor length Reynolds numbers  $Re_\lambda$  in the regions of the three wakes that we analyse range from about 150 to about 500.

In the following section we briefly describe the three turbulent wakes and the experimental data of Chen *et al.* (2021) that we use. These experiments were conducted in the low speed closed circuit wind tunnel of the *Laboratoire de Mécanique de Fluides de Lille* (LMFL) in 2020. Its test section is 2m wide by 1m high and 20m long and is transparent on all four sides for maximal use of optical techniques. A comprehensive description of these experiments can of course be found in Chen *et al.* (2021).

### 3. The wake experiments of Chen *et al.* (2021) and flow characteristics

Chen *et al.* (2021) collected 2D2C PIV data from three qualitatively different wakes generated with a simple single-parameter set-up. They measured the wake of two side-by-side identical square prisms of side-width  $H = 0.03\text{m}$  in small fields of view (SFVN) of size similar to the horizontal size of the prisms with a high magnification factor at different streamwise distances  $X_1 = NH$  from the middle point between the two square prisms. The three different wake regimes are obtained by varying the gap distance  $G$  between the middle points of each prism in the cross-stream direction (measured by spatial coordinate  $X_2$ ). The three different gap ratios  $G/H$  chosen by Chen *et al.* (2021) correspond to three qualitatively different flows in terms of dynamics, bistability, large-scale features and non-homogeneity as explained in Chen *et al.* (2021) and references therein. The resulting three wakes are illustrated in Fig. 1. The velocity fields in Fig. 1 come from a large field of view PIV also performed by Chen *et al.* (2021) mainly for integral length scale measurements and shown here for illustrative purposes only. We make use of some of their integral length scale measurements as reference length scales but we do not use their large field of view data. We only use some of their small field of view PIV data as they are spatially well resolved. The small fields of view SFVN with  $N$  from 2.5 to 20 are indicated in the figure. Their size is  $1H$  in the streamwise direction by  $0.9H$  in the cross-stream direction and their centre coincide with the geometric centreline ( $X_2 = 0$ ).

A dual-camera PIV set-up was used by Chen *et al.* (2021) for each one of the small fields of view. Two sCMOS cameras, one over the top and one under the bottom of the test section were aimed at the same small field of view so as to obtain two independent measurements of the same velocity field for PIV noise reduction. As comprehensively explained in Chen *et al.* (2021) and in Beaumard *et al.* (2024), this noise reduction method is a key step to obtain accurate dissipation rate estimates. The acquisition frequency was 5 Hz and 20000 velocity fields were captured for each measurement corresponding to about 67 min. The PIV analysis' final interrogation window size was  $24 \times 24$  pixels with about 58% overlap which corresponds to a  $312\mu\text{m}$  interrogation window which ranged from 4.5 to 2.5 times the Kolmogorov length scale  $\eta$  from nearest to farthest SFVN (i.e. with increasing  $N$ ). For all the small fields of view data used in the present paper, the interrogation window size is below  $3.2\eta$ .

Chen *et al.* (2021) acquired data for three incoming free stream velocities  $U_\infty = 5.0, 6.0, 7.35 \text{ m/s}$  corresponding to three values of the global Reynolds number  $Re_H \equiv$

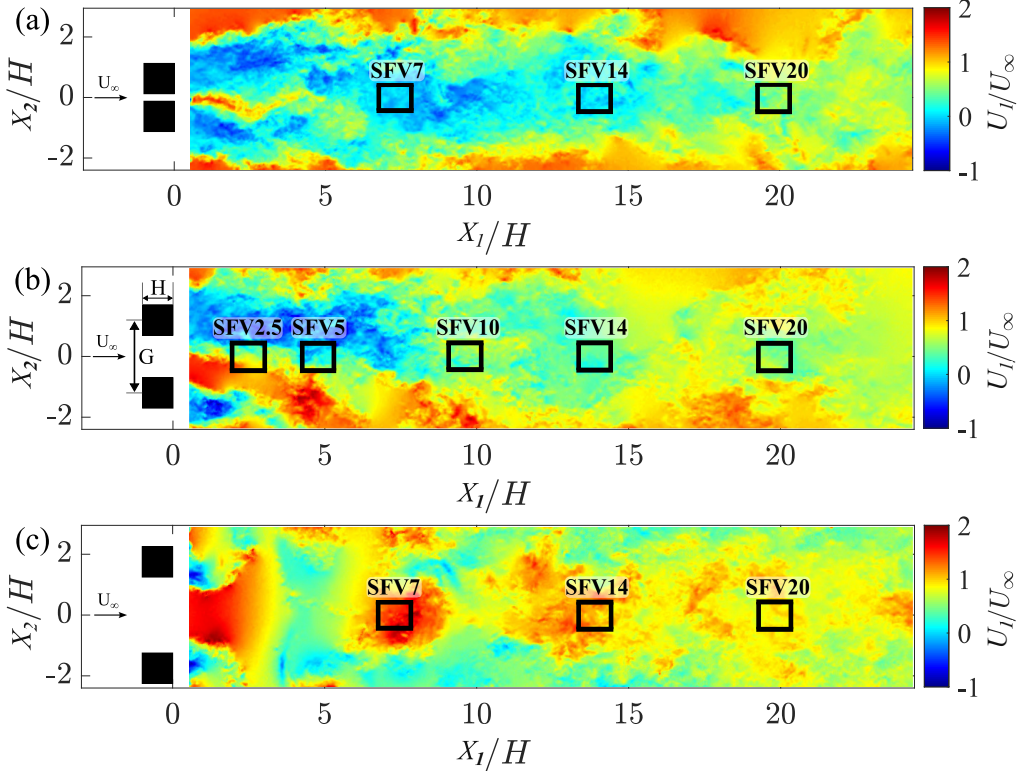


Figure 1: Example of normalised instantaneous streamwise velocity realisations  $U_1/U_\infty$  in the wakes generated by two square prisms (■) of side  $H$  separated by a gap  $G$  at  $Re_H = 1.0 \times 10^4$ . Flow patterns are shown for gap ratios (a)  $G/H = 1.25$ , (b)  $G/H = 2.4$  and (c)  $G/H = 3.5$ . 2D2C PIV data courtesy of Chen *et al.* (2021).

Case $G/H = 1.25$	SFV7	SFV14	SFV20
$Re_H (\times 10^4)$	1	1	1
$Re_\lambda$	142	321	381
$\langle \varepsilon \rangle (\text{m}^2 \cdot \text{s}^{-3})$	18.6	23.5	34.9
$\eta (\text{m})$	$120 \times 10^{-6}$	$113 \times 10^{-6}$	$102 \times 10^{-6}$
$\lambda (\text{m})$	$2.8 \times 10^{-3}$	$4.0 \times 10^{-3}$	$3.9 \times 10^{-3}$
$\langle \mathcal{L}_v \rangle / H$	0.98	1.4	1.4
$\langle \mathcal{L}_v \rangle / \lambda$	10.5	10.8	11.0
$L_I / \lambda$	2.1	1.5	1.2
			2.6
			2.7

Table 1: Flow characteristics for the available wake regions and global Reynolds numbers for case  $G/H = 1.25$ .

$U_\infty H / \nu = 1.0 \times 10^4, 1.2 \times 10^4$  and  $1.5 \times 10^4$ , respectively. The characteristics of the turbulence in each SFV $N$  are reported in tables 1, 2 and 3 for all available global Reynolds numbers for all cases  $G/H = 1.25$ ,  $G/H = 2.4$  and  $G/H = 3.5$ . The Kolmogorov length  $\eta \equiv (\nu^3 / \langle \varepsilon \rangle)^{1/4}$  and the Taylor length estimate  $\lambda = (10\nu K_h / \langle \varepsilon \rangle)^{1/2}$  have been computed using our estimation of the space-time average turbulent dissipation rate  $\langle \varepsilon \rangle$  (see following paragraph) and the space-time average horizontal one-point turbulent kinetic energy  $K_h \equiv \frac{1}{2} \langle u_1'^2 + u_2'^2 \rangle$ . The

Case $G/H = 2.4$	SFV2.5	SFV5	SFV10	SFV14	SFV20	
$Re_H (\times 10^4)$	1	1	1	1.2	1	1.2
$Re_\lambda$	260	266	185	186	148	164
$\langle \varepsilon \rangle (\text{m}^2 \cdot \text{s}^{-3})$	94.6	72.2	41.2	29.6	8.9	15.0
$\eta (\text{m})$	$80 \times 10^{-6}$	$85 \times 10^{-6}$	$98 \times 10^{-6}$	$106 \times 10^{-6}$	$144 \times 10^{-6}$	$126 \times 10^{-6}$
$\lambda (\text{m})$	$2.5 \times 10^{-3}$	$2.7 \times 10^{-3}$	$2.6 \times 10^{-3}$	$2.9 \times 10^{-3}$	$3.4 \times 10^{-3}$	$3.2 \times 10^{-3}$
$\langle \mathcal{L}_v \rangle / H$	$0.42 \pm 0.1$	$0.79 \pm 0.1$	0.92	0.94	0.94	0.96
$\langle \mathcal{L}_v \rangle / \lambda$	5.0	8.7	10.5	9.9	8.2	9.0
$L_I / \lambda$	2.6	2.3	1.3	0.9	1.1	1.6

Table 2: Flow characteristics for the available wake regions and global Reynolds numbers for case  $G/H = 2.4$ . The uncertainties are shown for the cases where the integral length scale varies more than 20% across the SFV.

Case $G/H = 3.5$	SFV7	SFV14			SFV20	
$Re_H (\times 10^4)$	1	1	1.2	1	1.2	1.5
$Re_\lambda$	183	129	167	118	135	160
$\langle \varepsilon \rangle (\text{m}^2 \cdot \text{s}^{-3})$	41.9	26.8	33.2	12.5	21.0	34.7
$\eta (\text{m})$	$98 \times 10^{-6}$	$109 \times 10^{-6}$	$103 \times 10^{-6}$	$132 \times 10^{-6}$	$116 \times 10^{-6}$	$102 \times 10^{-6}$
$\lambda (\text{m})$	$2.6 \times 10^{-3}$	$2.4 \times 10^{-3}$	$2.6 \times 10^{-3}$	$2.8 \times 10^{-3}$	$2.6 \times 10^{-3}$	$2.6 \times 10^{-3}$
$\langle \mathcal{L}_v \rangle / H$	0.74	0.64	0.67	0.58	0.60	0.62
$\mathcal{L}_v / \lambda$	8.5	7.9	7.7	6.2	6.8	7.3
$L_I / \lambda$	1.4	1.7	0.9	1.1	1.2	1.3

Table 3: Flow characteristics for the available wake regions and global Reynolds numbers for case  $G/H = 3.5$ .

angular brackets  $\langle \rangle$  represent a space average over the entire small field of view. The Taylor length-based Reynolds number has been computed as  $Re_\lambda = \sqrt{(2/3)K_h \lambda} / v$ . Both  $Re_\lambda$  and  $\lambda = (10vK_h / \langle \varepsilon \rangle)^{1/2}$  are under-estimated because they have been computed with  $K_h$  rather than  $\frac{1}{2} \langle u_1'^2 + u_2'^2 + u_3'^2 \rangle$  which is not accessible using the 2D2C PIV data of Chen *et al.* (2021).

To obtain the time-averaged turbulence dissipation rate  $\varepsilon$  we make use of the assumption of local axisymmetry around the streamwise ( $X_1$ ) axis which implies  $\varepsilon_3 = \varepsilon_2$  and therefore  $\varepsilon = \varepsilon_1 + 2\varepsilon_2$  (George & Hussein 1991). This local axisymmetry has been found to be a very good approximation for the calculation of  $\varepsilon$  both experimentally and numerically in numerous flows. In particular, Lefeuvre *et al.* (2014) found that this approximation yields accurate results of  $\varepsilon$  in the wake of a square cylinder. More importantly, Alves-Portela & Vassilicos (2022) achieved the same conclusions using Direct Numerical Simulations (DNS) for the same flows studied in this paper. We are therefore able to estimate the full turbulence dissipation rate  $\varepsilon$  from the 2D2C PIV data of (Chen *et al.* 2021) as they give access to  $\varepsilon_1$  and  $\varepsilon_2$ . This axisymmetric estimate has also been denoised using a technique based on a dual camera set-up (Chen *et al.* 2021; Foucaut *et al.* 2021).

We also include the space-averaged integral length scale  $\langle \mathcal{L}_v \rangle$  as a fraction of  $H$  and  $\lambda$  in tables 1, 2 and 3. The length scale  $\mathcal{L}_v$  was estimated by Chen *et al.* (2021) from the cross-stream velocity auto-correlation function in the streamwise direction as the integration of the streamwise velocity autocorrelation function in that same direction does not always

converge (Chen *et al.* 2021). Although Chen *et al.* (2021) reported some variations in the very near fields,  $\mathcal{L}_v$  remains fairly constant in each SFV $\mathcal{N}$  except for SFV2.5 and SFV5 of configuration  $G/H = 2.4$ . In terms of multiples of  $\langle \mathcal{L}_v \rangle$ , the SFV $\mathcal{N}$  locations are much closer to the prisms in the  $G/H = 1.25$  than in the other two cases. This is reflected in table 1 where  $\langle \mathcal{L}_v \rangle$  reaches values up to  $1.6H$  at SFV20 for instance.

Not only do these wakes exhibit distinct flow characteristics arising from their respective inlet conditions ( $G/H$  parameter), one should also expect the physics to be different in the near field where the turbulence increases with the streamwise distance compared to further downstream where the turbulence decreases with streamwise distance. The present work concentrates on the further downstream decaying wake regions, hence on SFV7, SFV14 and SFV20 for  $G/H = 3.5$ , SFV10, SFV14 and SFV20 for  $G/H = 2.4$  and SFV20 for  $G/H = 1.25$  (see Fig. 1). One can see in tables 1, 2 and 3 that the local Reynolds number  $Re_\lambda$  decreases from SFV7 to SFV14 to SFV20 for  $G/H = 3.5$  and from SFV10 to SFV14 to SFV20 for  $G/H = 2.4$ . The following one-point energy analysis confirms that one-point production is small in these SFV stations and that they are therefore in the downstream decaying region of the  $G/H = 3.5$  and  $G/H = 2.4$  flow cases. For flow case  $G/H = 1.25$ ,  $Re_\lambda$  actually increases from SFV7 to SFV14 to SFV20. Furthermore, the one-point energy analysis below suggests that SFV20 may not be in the decaying region of the  $G/H = 1.25$  wake. We nevertheless keep  $G/H = 1.25$  SFV20 in our study for comparison.

To further characterise the turbulence at the SFV locations of interest before starting our two-point energy analysis, we look at the one-point horizontal turbulent kinetic energy transport equation. Taking advantage of the up-down symmetry and statistical homogeneity in the spanwise direction (normal to the  $(X_1, X_2)$  plane), this equation reads

$$\overline{u_1} \frac{\partial \overline{K_h}}{\partial X_1} + \overline{u_2} \frac{\partial \overline{K_h}}{\partial X_2} - \mathcal{P} + \mathcal{T} = \mathcal{T}_p + \mathcal{D} - \varepsilon, \quad (3.1)$$

where  $\mathcal{P} = -\overline{u'_1 u'_1} \frac{\partial \overline{u_1}}{\partial X_1} - \overline{u'_1 u'_2} \frac{\partial \overline{u_1}}{\partial X_2} - \overline{u'_1 u'_2} \frac{\partial \overline{u_2}}{\partial X_1} - \overline{u'_2 u'_2} \frac{\partial \overline{u_2}}{\partial X_2}$  is the one-point turbulence production rate,  $\mathcal{T} = \frac{\partial}{\partial X_1} (\overline{u'_1 K_h}) + \frac{\partial}{\partial X_2} (\overline{u'_2 K_h})$  is the one-point turbulent diffusion rate and where  $\mathcal{T}_p$  and  $\mathcal{D}$  are the one-point pressure-velocity correlation and molecular diffusion terms respectively. Note that our 2D2C PIV enables full evaluations of  $\mathcal{P}$  and  $\mathcal{T}$  because of the spanwise homogeneity. We focus on three key terms,  $\mathcal{P}$ ,  $\mathcal{T}$  and  $\varepsilon$ , with particular emphasis on how the first two compare in magnitude to  $\varepsilon$ . Figure 2a shows  $\langle \mathcal{P} \rangle / \langle \varepsilon \rangle$  (the averaging being over the entire SFV) for all flow cases. At all SFV locations considered in the  $G/H = 3.5$  and  $G/H = 2.4$  wakes,  $\langle \mathcal{P} \rangle$  generally remains between 1-5% of  $\langle \varepsilon \rangle$  except for our closest station (SFV7) in the  $G/H = 3.5$  flow case where  $\langle \mathcal{P} \rangle$  approaches 10% of  $\langle \varepsilon \rangle$  and has a negative sign. This is in contrast with  $G/H = 1.25$  SFV20 where  $\langle \mathcal{P} \rangle$  is no longer negligible, reaching values up to 50% of  $\langle \varepsilon \rangle$  for  $Re_H = 1.0 \times 10^4$  (but positive). This sharp difference suggests that at our farthest measurement station (SFV20) the  $G/H = 1.25$  wake flow may not have yet entered the downstream decaying regime. In the following section we report that there are also significant differences in the two-point turbulent kinetic energy budget between  $G/H = 1.25$  SFV20 and the SFV stations that we consider in the decay regions of the  $G/H = 3.5$  and  $G/H = 2.4$  flow cases.

Figure 2b displays normalised space-averaged one-point turbulent diffusion rates  $\langle \mathcal{T} \rangle / \langle \varepsilon \rangle$  and compares them with  $\langle \mathcal{P} \rangle / \langle \varepsilon \rangle$  for the  $G/H = 3.5$  and  $G/H = 2.4$  wakes. We find that  $\langle \mathcal{T} \rangle$  ranges from approximately 15% to 25% of  $\langle \varepsilon \rangle$ , consistently exceeding  $\langle \mathcal{P} \rangle$  by a factor close to three or more across all SFV stations in the decay regions of these two wakes. Whereas average production is small,  $\langle \mathcal{T} \rangle$  is significant, which is a clear sign of non-homogeneity, a non-homogeneity which may qualify as “non-producing non-homogeneity”. Notably,  $\langle \mathcal{T} \rangle$

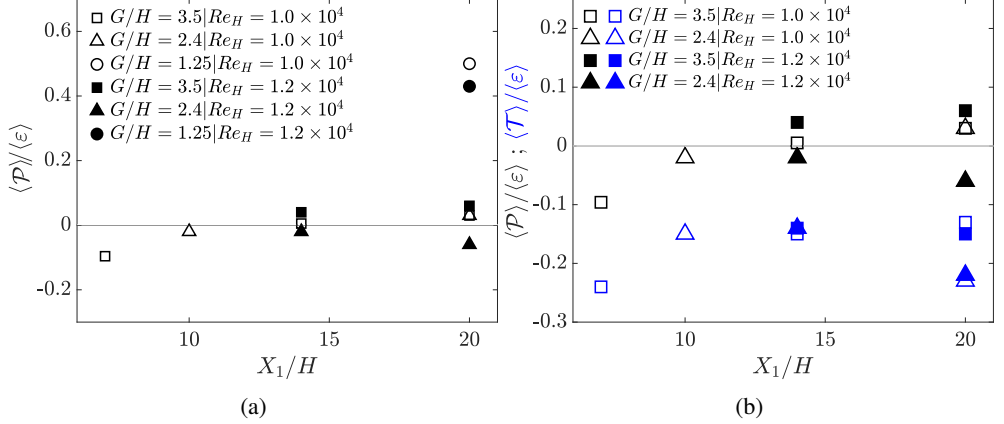


Figure 2: Average values of one-point production  $\langle \mathcal{P} \rangle$  (a) and turbulent diffusion  $\langle \mathcal{T} \rangle$  (b) normalised by the average dissipation rate  $\langle \varepsilon \rangle$  across the studied SFVs for two  $Re_H$  values.

has a negative sign, indicating that, on average, turbulence is transporting turbulent kinetic energy into these SFVs.

The SFV20 station in the  $G/H = 1.25$  wake is very different as  $\langle \mathcal{T} \rangle$  is positive there, specifically  $\langle \mathcal{T} \rangle / \langle \varepsilon \rangle = 1.75$  and  $1.67$  for  $Re_H = 1.0 \times 10^4$  and  $1.2 \times 10^4$  respectively. This is a station with a non-homogeneity caused by both turbulent production and turbulent diffusion where turbulence is transporting turbulent kinetic energy outside SFV20.

To quantify the non-homogeneity characteristic of turbulent diffusion, a length scale is introduced and computed within the SFVs. To the authors' knowledge, no prior studies have characterised the degree of such non-homogeneity through a dedicated length scale. Although the Corrsin length, as recently used in (Kaneda 2020; Chen *et al.* 2021) for example, distinguishes between scales influenced or not influenced by mean flow gradients (and therefore also potentially by turbulence production), it does not capture the degree of non-homogeneity related to turbulent diffusion in the near-absence of production. Length scales such as  $L_{IK_1} \equiv \frac{K_h}{|\frac{\partial K_h}{\partial x_1}|}$ ,  $L_{IK_2} \equiv \frac{K_h}{|\frac{\partial K_h}{\partial x_2}|}$  and  $L_{IK} = \frac{k_h}{|\nabla K_h|}$  characterise the non-homogeneity of the one-point turbulent kinetic energy. In the seven regions in total considered here within the three turbulent wakes  $G/H = 1.25, 2.4, 3.5$  we find  $L_{IK_j} \gg L_{IK} \gg H$  for  $j = 1, 2$  with values that are one to two orders of magnitude larger than  $H$  for  $L_{IK_j}$  across each SFV and between 6 to 15 times  $H$  for  $\langle L_{IK} \rangle$ . This suggests that the turbulent kinetic energy is not strongly non-homogeneous in our SFVs. We therefore propose a length scale based on the one-point turbulent diffusion of kinetic energy, defined as follows:

$$L_I = \frac{\langle |u'_2 K_h| \rangle}{\langle \left| \frac{\partial}{\partial x_j} u'_j K_h \right| \rangle} \quad (3.2)$$

with an implicit sum over  $j = 1, 2$ . The space-average in this definition is over an SFV area in the present paper, but can be generalised (or perhaps even lifted) for other studies. A turbulence with little turbulence production but significant turbulent diffusion may be considered to be locally homogeneous over local regions of size smaller than  $L_I$ . In the extreme case of homogeneous turbulence in an infinite or periodic domain,  $L_I$  is infinite everywhere.

Values of  $L_I$  are reported in tables 1, 2 and 3 and are compared to the corresponding SFV's Taylor length. For all SFV/N locations, irrespective of type of wake, position in the wake

and even global or local Reynolds number, the values of  $L_I$  are comparable to those of  $\lambda$  and well below the integral length scale. These findings confirm that non-homogeneity related to turbulent diffusion is present throughout all wake regions down to scales of the order of the Taylor length  $\lambda$ . Having established one-point characteristics of the various wake regions, the following section addresses the budget (2.2) with particular attention to the inter-scale and inter-space transfer rates of horizontal two-point turbulent kinetic energy which constitute the core subject of this study.

#### 4. Two-point statistics results

Given the up-down symmetry in the spanwise direction (i.e. along the direction normal to the horizontal  $(X_1, X_2)$  plane, the spanwise components of  $\bar{\mathbf{u}_X}$  and  $\delta\bar{\mathbf{u}}$  are zero. Hence, the linear transport rate (2.3) can be fully determined from 2D2C measurements in the  $(X_1, X_2)$  plane if we limit ourselves to  $\mathbf{r} = (r_1, r_2, 0)$ . Statistical homogeneity in the spanwise direction implies that the gradients  $\nabla_{\mathbf{X}}\delta\bar{u}_i$  and  $\nabla_{\mathbf{r}}\delta\bar{u}_i$  have zero spanwise components for any index  $i$ , thereby implying that the two-point turbulence production rate (2.4) can also be fully determined from 2D2C measurements in the  $(X_1, X_2)$  plane. Spanwise statistical homogeneity also implies  $\frac{\partial}{\partial X_3}\overline{u'_{X_3}\delta K_h} = 0$  so that (2.5) reduces to

$$T_X \equiv \frac{\partial}{\partial X_1}\overline{u'_{X_1}\delta K_h} + \frac{\partial}{\partial X_2}\overline{u'_{X_2}\delta K_h}, \quad (4.1)$$

where  $\mathbf{X} = (X_1, X_2, X_3)$  and  $\mathbf{u}'_{\mathbf{X}} = (u'_{X_1}, u'_{X_2}, u'_{X_3})$ .

The only terms in the scale-by-scale turbulent kinetic energy budget (2.2) which cannot be fully determined from 2D2C PIV measurements in the  $(X_1, X_2)$  plane even for  $r_3 = 0$  are the inter-scale transfer rate  $\Pi_h$  defined in equation (2.6), the two-point pressure-velocity term  $T_p$  defined in equation (2.7) and the viscous diffusion rate  $D$  defined in equation (2.8). Whilst  $T_p$  is not at all accessible by such measurements, the part  $\Pi_r \equiv \frac{\partial}{\partial r_1}\overline{\delta u'_1\delta K_h} + \frac{\partial}{\partial r_2}\overline{\delta u'_2\delta K_h}$  of  $\Pi_h$  is accessible whereas the part  $\Pi_z \equiv \frac{\partial}{\partial r_3}\overline{\delta u'_3\delta K_h}$  is not. Concerning  $D$ , most of it is accessible for  $r_3 = 0$  except  $D_z \equiv \frac{\partial^2}{\partial r_3^2}\overline{\delta K_h}$ , see equation (2.8).

In summary, the scale-by-scale budget of the horizontal two-point turbulent kinetic energy can be expressed as

$$L_T - P + T_X + \Pi_r + \Pi_z = T_p + D_r + D_z - \tilde{\varepsilon}_1 - \tilde{\varepsilon}_2, \quad (4.2)$$

where  $D_r \equiv D - D_z$  and  $\Pi_r \equiv \Pi_h - \Pi_z$ . Every term in (Eq. 4.2) can be fully obtained from the small field of view 2D2C PIV measurements of Chen *et al.* (2021) for  $\mathbf{r} = (r_1, r_2, 0)$  except  $\Pi_z$ ,  $T_p$  and  $D_z$ . In this paper we primarily study the space-time average turbulence transfer rates  $\langle T_X \rangle$  and  $\langle \Pi_r \rangle$ . We verified that the spatial average does not impact our results by replacing the average  $\langle \rangle$  over the entire small field of view by an average over any straight line  $X_1 = \text{const}$  or  $X_2 = \text{const}$  within the small field of view and checking that the same conclusions presented here are reached, albeit with less statistical convergence (see examples of such checks for  $\langle T_X \rangle$  and  $\langle \Pi_r \rangle$  in Appendix B).

Following Larssen & Vassilicos (2023), we ask whether the accessible part,  $\langle \Pi_r \rangle$ , of the average inter-scale turbulence transfer rate counteracts or cooperates with the average inter-space turbulence transfer rate  $\langle T_X \rangle$ , and how they both compare with the average turbulence dissipation rate  $\langle \varepsilon \rangle$  in terms of magnitude. The  $\Pi_r$  part of the inter-scale turbulence transfer rate  $\Pi_h$  is the part which is fully determined by the horizontal velocity field without any direct influence from the spanwise (out-of-plane) velocity field, very much like  $T_X$ . Note that space-time averages are used to achieve statistical convergence of the third order statistics

involved in these transfer rates (over 20,000 uncorrelated samples and over the entire field of view). How do these average transfer rates depend on  $r_1$  for  $r_2 = r_3 = 0$  and on  $r_2$  for  $r_1 = r_3 = 0$  and over what scale-ranges? We answer these questions and also calculate  $\langle L_T \rangle$  and  $\langle P \rangle$  to complement the analysis which is carried out in the decay region around the centreline of the three qualitatively different turbulent wakes described in the previous section. Note that in the SFV14 and SFV20 locations of the  $G/H = 2.4$  and  $G/H = 3.5$  wakes, Chen & Vassilicos (2022) have shown, using the exact same data used here, that the longitudinal and transverse second order structure functions vary with two-point separation  $r_1$  as  $r_1^{2/3}$  in an inertial subrange of scales  $r_1$ . They also found that these two structures functions depart from this scaling and evolve faster than  $r_1^{2/3}$  at the SFV20 location of the  $G/H = 1.25$  wake.

The horizontal two-point turbulent kinetic energy  $\overline{\delta K_h}$  is the sum of these structure functions and thus scales in the same manner for  $r_1$  and  $r_2$  as shown in Appendix A where we also show that there is a departure from the 2/3 power law at the SFV7 location of the  $G/H = 3.5$  wake. We now present our results on the average inter-scale and inter-space transfer rates, starting below with an overview of the main results detailed in the following sub-sections. This overview is intended to help the reader's focus when reading through the discussion of our results one wake at a time in the following sub-sections. We also advance some hypotheses on which we base a tentative qualitative explanation of some of our results.

As can be seen in the subsequent figures, in all the small fields of view in the decaying wake region of both  $G/H = 3.5$  and  $G/H = 2.4$  turbulent wakes as well as in SFV20 of the  $G/H = 1.25$  turbulent wake, we find that  $\langle T_x \rangle$  is positive whilst  $\langle \Pi_r \rangle$  is negative for all accessible length-scales  $r_1 \neq 0$  and  $r_2 \neq 0$  at the very least smaller or equal to  $\langle \mathcal{L}_v \rangle$ . This means that, on average, scales smaller than  $r_1$  or  $r_2$  within the small field of view gain horizontal two-point turbulent kinetic energy via the interscale transfers but also lose it to the neighbouring physical space outside the small field of view by turbulent diffusion. The subsequent figures also show that, in all these cases, the fully horizontal inter-scale transfer rate  $\langle \Pi_r \rangle$  is significantly larger or sometimes approximately equal in magnitude to  $\langle \varepsilon \rangle$  over all accessible length scales, or sometimes a significant range of them. Furthermore, the subsequent figures make it clear that the two-point turbulent diffusion is not at all negligible compared to  $\langle \varepsilon \rangle$  for all length scales  $r_1$  or  $r_2$  larger than a fraction of the Taylor length and, at the very least, smaller than  $\langle \mathcal{L}_v \rangle$ . (Note that  $\mathcal{L}_v$  varies by at most 8% of  $\langle \mathcal{L}_v \rangle$ , and typically much less, within each one of the SFVs we consider.) Non-homogeneity is therefore present at all inertial length scales all the way down to viscosity-affected length scales for all of our local Reynolds numbers  $Re_\lambda$  which range up to nearly 500, in agreement with the theory of Chen & Vassilicos (2022) and of Beaumard *et al.* (2024) which predicts that non-homogeneity can be present over the entire inertial range even in the limit of infinite Reynolds number.

Non-homogeneity all the way down to the smallest scales is not inconceivable in the presence of inter-scale turbulent energy transfers. The argument runs as follows. An increase in inter-space turbulence transfer can remove energy from the inter-scale transfer process to smaller scales. If we hypothesise, for simplicity of argument, that the turbulence dissipation rate is somehow independently set by some mechanism in the flow, then the rate of inter-scale transfer of the remaining energy may accelerate to ensure the turbulence dissipation rate is met. If this leads to an increase of the inter-scale turbulence transfer, the energy available for turbulent diffusion at a given scale may reduce which could bring the inter-space turbulence transfer rate down at that scale. (This is a two-point analogue of the observation made by Alexakis (2023) that the turbulence dissipation (hence the turbulent cascade) can reduce, even inhibit, one-point turbulent diffusion.) Going back to the start of our argument, a

reduction in inter-space turbulence transfer may have the inverse effect of an increase and may decelerate the rate of inter-scale turbulence transfer to ensure the turbulence dissipation rate is met. In turn, this may increase the energy available for turbulent diffusion and bring the inter-space turbulence transfer rate back up. A balance between the two transfers may consequently be achieved so that none of them vanishes and non-homogeneity persists at all scales irrespective of Reynolds number. Of course, the mechanism setting the turbulence dissipation rate is likely to interact with the interplay between inter-scale and inter-space transfers in which case a balance may somehow be dynamically reached between these two transfer mechanisms and the turbulence dissipation. We stress that this is an argument for plausibility not a definitive explanation of the small-scale non-homogeneity reported in the following sub-sections. We leave this explanation and the important question of what sets the local turbulence dissipation rate in non-homogeneous turbulence (see Lumley 1992) for future investigation.

A particular aspect of the small-scale non-homogeneity observed in the subsequent figures is that  $\langle T_X \rangle$  is uniformly positive at all length scales  $r_1$  and  $r_2$  equal to or smaller than  $\langle \mathcal{L}_v \rangle$  and in most cases even above  $\langle \mathcal{L}_v \rangle$ . On the other hand, the one point turbulent diffusion rate  $\mathcal{T}$  is negative in all SFV stations except SFV20 in the  $G/H = 1.25$  where it is positive. The two-point inter-space transfer rate can be decomposed as  $\langle T_X \rangle = \langle \mathcal{T}^+ \rangle + \langle \mathcal{T}^- \rangle + \text{Corr} \approx 2\langle \mathcal{T} \rangle + \text{Corr}$  where  $\mathcal{T}^\pm \equiv \mathcal{T}(\mathbf{X} \pm \mathbf{r})$  and  $\text{Corr}$  is the space-average over the small field of view of the sum of all two-point correlation terms making up  $\langle T_X \rangle$ . At the SFV20 station of the  $G/H = 1.25$  wake,  $\langle T_X \rangle$  and  $\mathcal{T}$  are both positive and, as shown in Appendix C,  $\text{Corr}$  is negative and decreasing in magnitude with increasing  $r_1$  and  $r_2$ . At all the other six stations considered here,  $\text{Corr}$  is positive and generally non-increasing in magnitude with increasing  $r_1$  and  $r_2$  above  $\lambda$ . This is a striking illustration of the difference that we observe in terms of qualitatively different two-point correlations between the scale-by-scale non-homogeneity for SFV20  $G/H = 1.25$  and the scale-by-scale non-homogeneity at the other six stations considered in the  $G/H = 2.4$  and  $G/H = 3.5$  wakes. The explanation of this difference requires a more comprehensive analysis of our turbulent wakes which goes beyond the present study.

We now give a detailed presentation of our results in the following subsections, one gap ratio  $G/H$  value at a time. (An even more detailed presentation of the inter-space energy transfer rate  $\langle T_X \rangle$  in terms of its decomposition into a streamwise transfer rate  $\langle \frac{\partial}{\partial X_1} \overline{u'_1 \delta K_h} \rangle$  and a cross-stream transfer rate  $\langle \frac{\partial}{\partial X_2} \overline{u'_2 \delta K_h} \rangle$  is presented in Appendix B where it is shown that both are positive across a wide range of length-scales all the way down to the Taylor length.)

#### 4.1. Horizontal two-point turbulent energy transfer rates in the $G/H = 3.5$ wake

In Fig. 3 we plot normalised inter-scale and inter-space energy transfer rates, denoted as  $\langle \Pi_r \rangle^* \equiv \langle \Pi_r \rangle / \langle \varepsilon \rangle$  and  $\langle T_X \rangle^* \equiv \langle T_X \rangle / \langle \varepsilon \rangle$  respectively, for SFV20 in the  $G/H = 3.5$  turbulent wake for the three available global Reynolds numbers  $Re_H$ . For all accessible values of  $r_1$  and  $r_2$  up to significantly above  $\langle \mathcal{L}_v \rangle$ ,  $\langle \Pi_r \rangle^* < 0$  and  $\langle T_X \rangle^* > 0$ , and  $\langle T_X \rangle^*$  increases as either  $r_1$  or  $r_2$  decrease towards  $\lambda$  or  $\lambda/2$  where it reaches its maximum at a value of about 0.5 or 0.6 depending on  $Re_H$ .  $\langle \Pi_r \rangle^*$  also increases in magnitude as either  $r_1$  or  $r_2$  decrease towards  $\lambda$  where it reaches its minimum at a value of about -1.1 for  $Re_H = 1.0 \times 10^4$  and  $1.2 \times 10^4$  and of about -1.4 for  $Re_H = 1.5 \times 10^4$ . Whilst  $\langle T_X \rangle^*$  does not vary significantly with  $Re_H$  in the small range of  $Re_H$  values considered,  $-\langle \Pi_r \rangle^*$  is significantly larger for  $Re_H = 1.5 \times 10^4$  than for  $Re_H = 1.0 \times 10^4$  and  $1.2 \times 10^4$  over all  $r_1$  scales and most  $r_2$  scales under  $\langle \mathcal{L}_v \rangle$ . Note that  $-\langle \Pi_r \rangle^*$  is larger than 1 for either  $r_1$  or  $r_2$  between  $\lambda/2$  and  $\langle \mathcal{L}_v \rangle/3$ , i.e. over the inertial range.

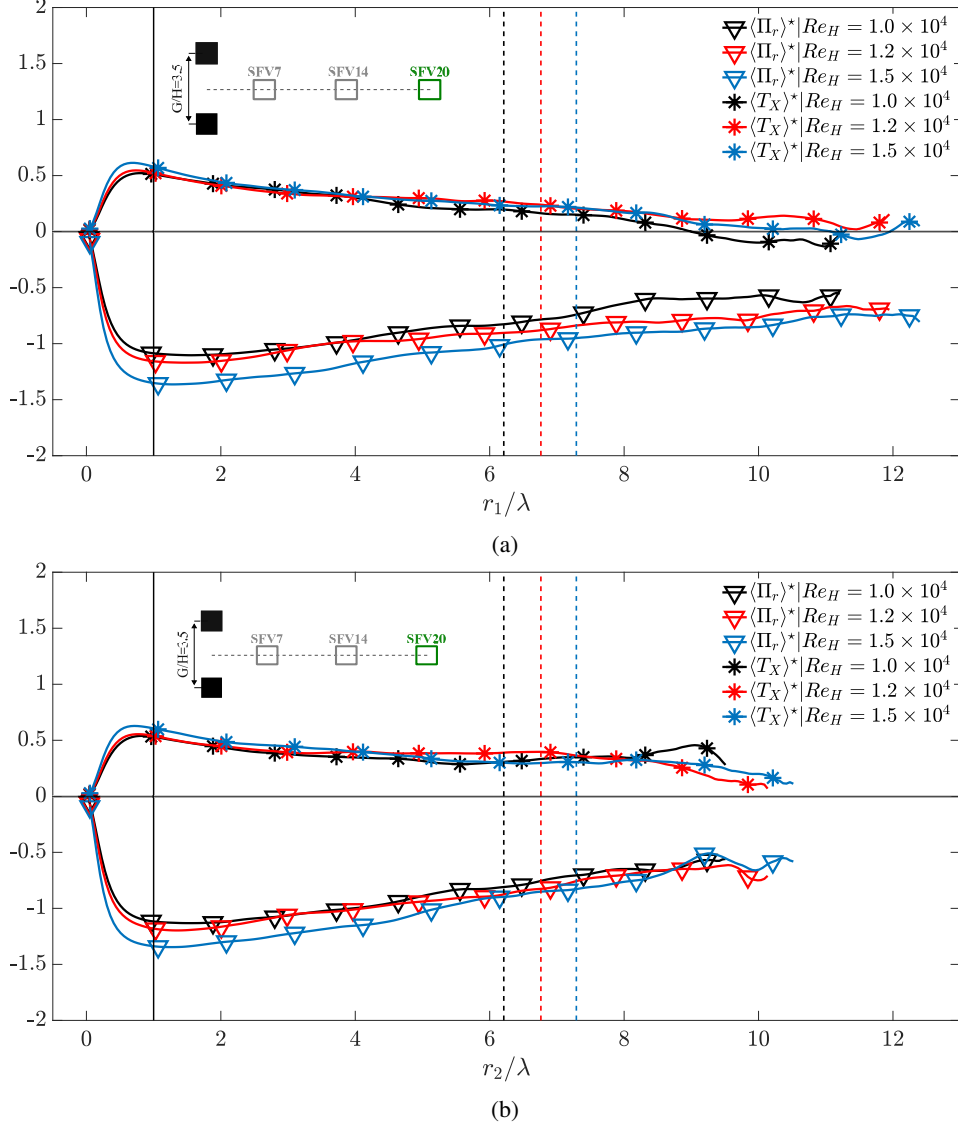


Figure 3: Normalised average scale-by-scale energy transfer rates in scale  $\langle \Pi_r \rangle^*$  and in physical  $\langle T_X \rangle^*$  space for configuration  $G/H = 3.5$  SFV20. Plots are shown for separations scales in the streamwise (a) and in the cross-stream (b) direction. Vertical dashed lines:  $\langle \mathcal{L}_v \rangle / \lambda$ . Only 1/20 of the markers are shown for clarity and a sketch is displayed to depict the  $G/H$  and SFV (green box) probed here. The same is done in the following figures.

The same plots are shown in Fig. 4 and Fig. 5 but for SFV14 and SFV7, respectively and the same observations are made. In particular,  $\langle T_X \rangle^*$  is equal to or larger than 0.4 at  $r_1 = \lambda/2$  and  $r_2 = \lambda/2$  and equal to or larger than 0.5 at  $r_1 = \lambda/2$  and  $r_2 = \lambda/2$  in all three small fields of view for all available global Reynolds numbers. The turbulence is therefore invariably very significantly non-homogeneous at the smallest turbulent length-scales. However, one also observes the following quantitative differences.

(i) There is a much greater sensitivity on  $Re_H$  at SFV14 than SFV20 which are the two fields of view for which two values of  $Re_H$  are available. The normalised average two-

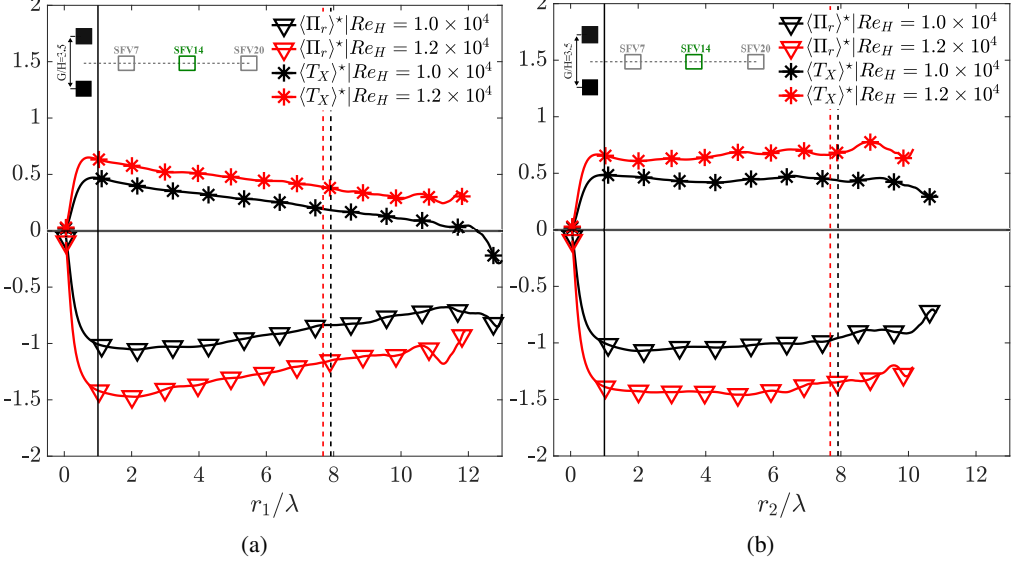


Figure 4: Normalised average scale-by-scale energy transfer rates in scale  $\langle \Pi_r \rangle^*$  and in physical  $\langle T_X \rangle^*$  space for configuration  $G/H = 3.5$  SFV14 at  $Re_H = 1.0$  and  $1.2 \times 10^4$ . Plots are shown for separations scales in the streamwise (a) and in the cross-stream (b) direction.

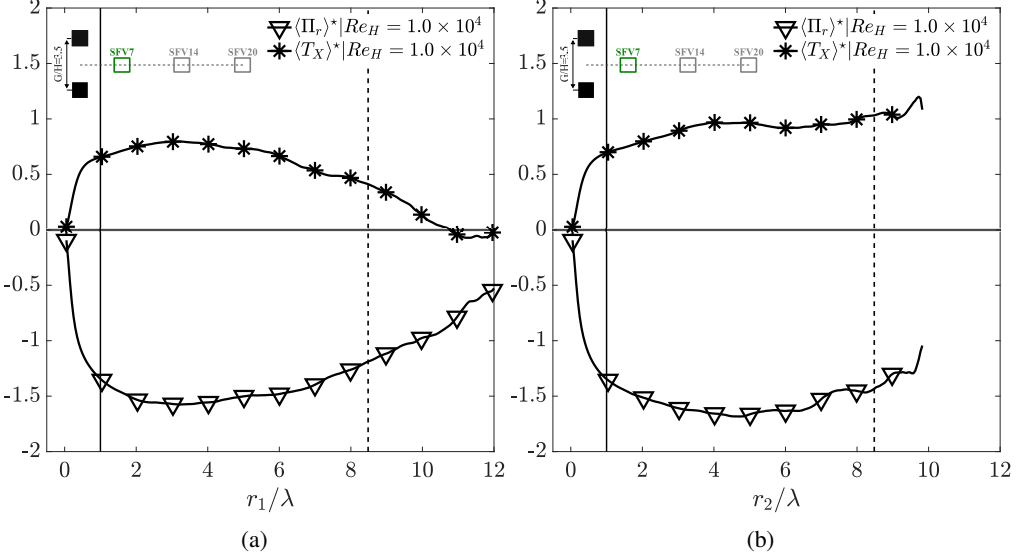


Figure 5: Normalised average scale-by-scale energy transfer rates in scale  $\langle \Pi_r \rangle^*$  and in physical  $\langle T_X \rangle^*$  space for configuration  $G/H = 3.5$  SFV7 at  $Re_H = 1.0 \times 10^4$ . Plots are shown for separations scales in the streamwise (a) and in the cross-stream (b) direction.

point inter-scale and inter-space transfer rates are approximately the same at SFV20 for  $Re_H = 1.0 \times 10^4$  and  $Re_H = 1.2 \times 10^4$  but they both increase very significantly in magnitude with this 20% jump in  $Re_H$  at SFV14.

(ii) At constant  $Re_H$ ,  $\langle \Pi_r \rangle^*$  and  $\langle T_X \rangle^*$  increase in magnitude as the small field of view gets closer to the square prisms along the centreline and the local  $Re_\lambda$  increases appreciably,

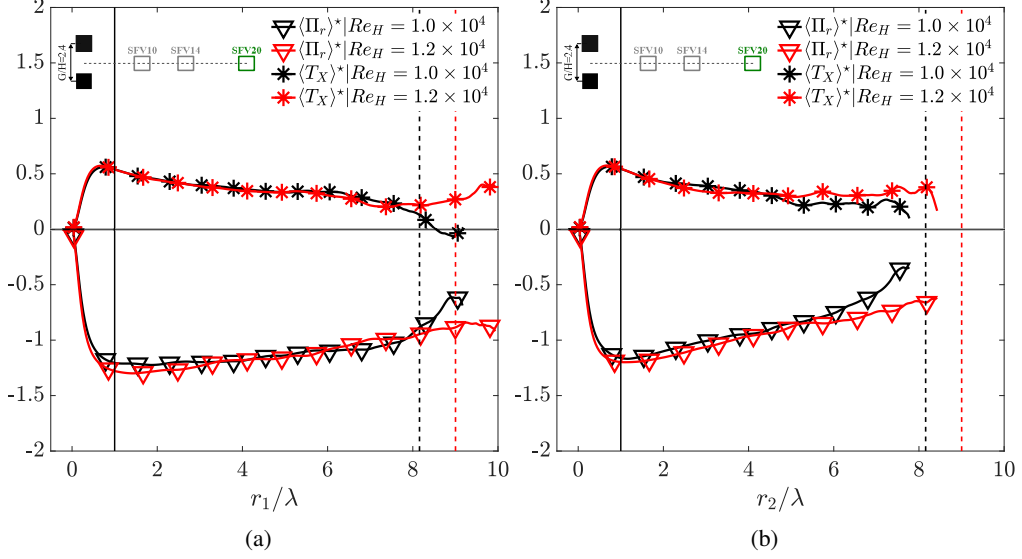


Figure 6: Normalised average scale-by-scale energy transfer rates in scale  $\langle \Pi_r \rangle^*$  and in physical  $\langle T_X \rangle^*$  space for configuration  $G/H = 2.4$  SFV20 at  $Re_H = 1.0$  and  $1.2 \times 10^4$ . Plots are shown for separations scales in the streamwise (a) and in the cross-stream (b) direction.

i.e. from SFV20 ( $Re_\lambda = 135$ ) to SFV14 ( $Re_\lambda = 167$ ) for  $Re_H = 1.2 \times 10^4$  and from SFV14 ( $Re_\lambda = 129$ ) to SFV7 ( $Re_\lambda = 183$ ) for  $Re_H = 1.0 \times 10^4$ . (There is no significant increase in  $Re_\lambda$  from SFV20 to SFV14 for  $Re_H = 1.0 \times 10^4$  and no significant change in the  $r_1$  and  $r_2$  profiles of  $\langle \Pi_r \rangle^*$  and  $\langle T_X \rangle^*$ .)

(iii) From SFV20 ( $Re_\lambda = 135$ ) to SFV14 ( $Re_\lambda = 167$ ) for  $Re_H = 1.2 \times 10^4$ , there is a tendency for  $\langle \Pi_r \rangle^*$  and  $\langle T_X \rangle^*$  to get closer to constant (near  $-1.5$  for  $\langle \Pi_r \rangle^*$  and near  $0.6$  for  $\langle T_X \rangle^*$ ) with either  $r_1$  or  $r_2$  in the inertial range between  $\lambda$  and  $\langle \mathcal{L}_v \rangle$ . There may be a similar but less well-defined tendency from SFV14 ( $Re_\lambda = 129$ ) to SFV7 ( $Re_\lambda = 183$ ) for  $Re_H = 1.0 \times 10^4$ .

Let us now consider a different turbulent wake by decreasing the gap ratio from  $G/H = 3.5$  to  $G/H = 2.4$ .

#### 4.2. Horizontal two-point turbulent energy transfer rates in the $G/H = 2.4$ wake

If one compares Figs. 3 and 6 (same SFV, different wake), the following remarks can be made. The  $r_1$  and  $r_2$  profiles of  $\langle \Pi_r \rangle^*$  and  $\langle T_X \rangle^*$  at SFV20 are very similar in the  $G/H = 2.4$  and  $G/H = 3.5$  turbulent wakes for the two global Reynolds numbers  $Re_H = 1.0 \times 10^4$  and  $Re_H = 1.2 \times 10^4$ , except that the local  $Re_\lambda$  values and  $\langle \mathcal{L}_v \rangle/\lambda$  ratios are higher for  $G/H = 2.4$  at the same  $Re_H$ . Our observations and conclusions for SFV20  $G/H = 2.4$  and SFV20  $G/H = 3.5$  are therefore the same (even quantitatively bearing in mind the  $Re_\lambda$  difference) for these two global Reynolds numbers.

In Fig. 7 we plot the  $r_1$  and  $r_2$  profiles of  $\langle \Pi_r \rangle^*$  and  $\langle T_X \rangle^*$  closer to the square prisms along the centreline, at SFV14 and SFV10. There is only one global Reynolds number available for each one of these small fields of view,  $Re_H = 1.2 \times 10^4$  for SFV14 and  $Re_H = 1.0 \times 10^4$  for SFV7 but  $Re_\lambda \approx 185$  for both. Whilst the inter-scale and inter-space transfer rates behave at SFV14 more or less as they do at SFV20 for  $G/H = 2.4$  (see Fig. 6), a substantial difference appears at the SFV10 station of the  $G/H = 2.4$  wake compared to all other stations examined in this paper in both the  $G/H = 2.4$  and  $G/H = 3.5$  wakes. It is the only one of these stations

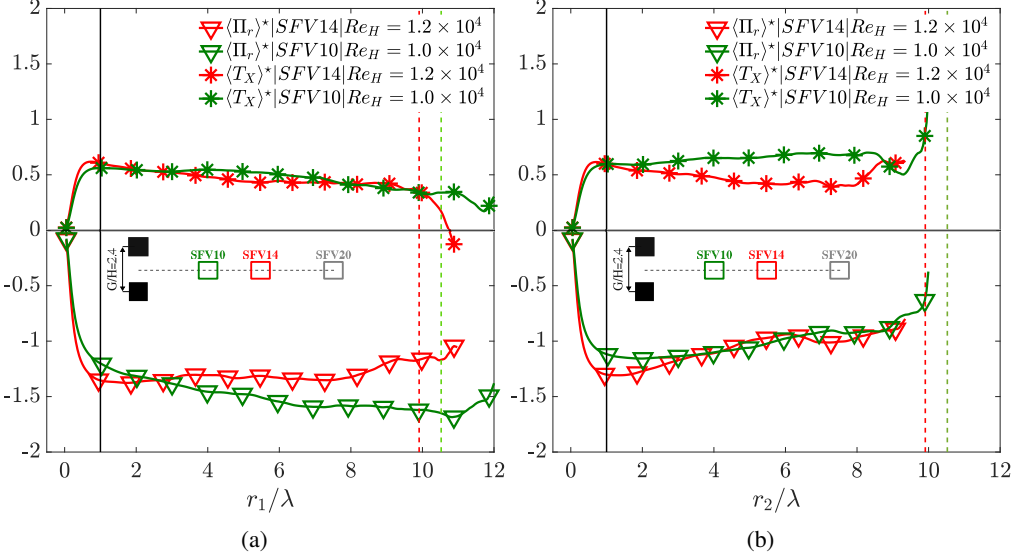


Figure 7: Normalised average scale-by-scale energy transfer rates in scale  $\langle \Pi_r \rangle^*$  and in physical  $\langle T_X \rangle^*$  space for configuration  $G/H = 2.4$  SFV14 at  $Re_H = 1.2 \times 10^4$  and SFV10 at  $Re_H = 1.0 \times 10^4$ . Plots are shown for separations scales in the streamwise (a) and in the cross-stream (b) direction.

where  $\langle \Pi_r \rangle^*$  and  $\langle T_X \rangle^*$  decrease monotonically together with increasing  $r_1$  and where  $\langle \Pi_r \rangle^*$  and  $\langle T_X \rangle^*$  increase monotonically together with increasing  $r_2$ . This difference is particularly striking by comparison to the SFV14 station of the same wake at a 20% higher global Reynolds number even though they both have the same  $Re_\lambda$  (see Fig. 7). Note, however, that in line with the other stations in the  $G/H = 3.5$  and  $G/H = 2.4$  wakes,  $\langle \Pi_r \rangle^*$  is particularly high in magnitude, between  $-1$  to  $-1.6$  in the inertial range  $\lambda$  to  $\langle \mathcal{L}_v \rangle$ . Furthermore,  $\langle T_X \rangle^*$  is consistently above  $0.3$  and it is equal to or larger than  $0.5$  at  $r_1 = \lambda/2$  and  $r_2 = \lambda/2$ . Once again, the turbulence is very significantly non-homogeneous at the smallest, and in fact viscosity-affected, turbulent length-scales. There is clearly no tendency towards local homogeneity at small enough turbulent length scales in any of the small fields of view in the centreline decay region of both  $G/H = 3.5$  and  $G/H = 2.4$  turbulent wakes and for all available global Reynolds numbers.

#### 4.3. The other terms in the scale-by-scale budget

In all the SFV $\mathcal{N}$  stations of the  $G/H = 2.4$  and  $G/H = 3.5$  turbulent wakes that we examined except SFV10 for  $G/H = 2.4$ ,  $\langle \Pi_r \rangle^*$  ranges from around  $-1$  to  $-1.5$  and remains constant or increases with increasing  $r_1$  or  $r_2$  whereas  $\langle T_X \rangle^*$  is close to  $0.5$  and remains constant or decreases with increasing  $r_1$  or  $r_2$ . Consequently,  $\langle \Pi_r \rangle^* + \langle T_X \rangle^*$  remains constant over the inertial range  $\lambda$  to  $\langle \mathcal{L}_v \rangle$  as shown in Fig. 8 except for SFV10,  $G/H = 2.4$ . This constant is between  $-0.6$  and  $-1.0$  depending on wake and location in the decaying wake.

As already mentioned, the linear transport rate  $L_T$  and the two-point turbulence production rate  $P$  are fully accessible from the 2D2C PIV data in our disposal. We find that they make a small contribution to the scale-by-scale energy budget (4.2) in all the SFV $\mathcal{N}$  stations of the  $G/H = 2.4$  and  $G/H = 3.5$  turbulent wakes examined in the present work except SFV10 for  $G/H = 2.4$ . This can be seen in Fig. 9 which shows that  $\langle L_T - P + T_X + \Pi_r \rangle / \langle \varepsilon \rangle$  is approximately constant in the inertial range  $\lambda$  to  $\langle \mathcal{L}_v \rangle$  with a constant which is between  $-0.7$  and  $-1.3$  in the  $r_1$  inertial range and between  $-0.5$  and  $-1.0$  in the  $r_2$  inertial range, with

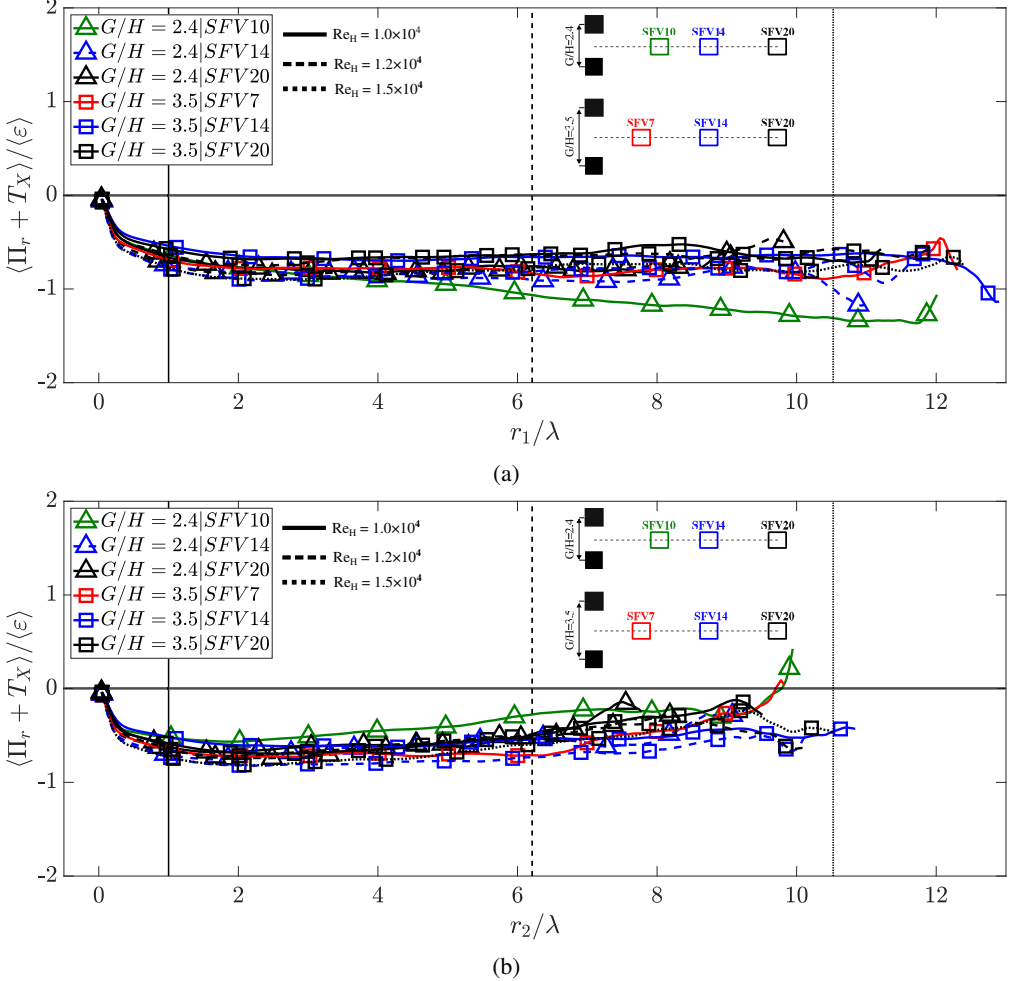


Figure 8: Normalised scale-by-scale plots of the sum of interscale and interspace small scale energy transfer rate  $\langle \Pi_r + T_X \rangle / \langle \varepsilon \rangle$ . Results are shown for separations scales in the streamwise (a) and in the cross-stream (b) directions. The vertical dashed and dotted lines represent the smallest and largest integral length scales for the SFVs, respectively.

*SFV10,  $G/H = 2.4$  being the one exception.* It is worth pointing out that the scale-by-scale energy budget (4.2) implies  $\langle L_T - P + T_X + \Pi_r \rangle \approx \langle T_p \rangle - \langle \Pi_z \rangle - \langle \varepsilon_1 \rangle - \langle \varepsilon_2 \rangle$  for  $r_1, r_2 > \lambda$ , suggesting the perhaps remarkable balance

$$\langle T_p \rangle - \langle \Pi_z \rangle \sim \langle \varepsilon \rangle \quad (4.3)$$

in the inertial  $r_1$  and  $r_2$  ranges, again with the one SFV10,  $G/H = 2.4$  exception.

#### 4.4. The SFV20 station in the $G/H = 1.25$ wake

The exceptional SFV10 station in the  $G/H = 2.4$  turbulent wake is at or close to the border between the near field where the turbulence and  $Re_\lambda$  increase and the subsequent field where the turbulence and  $Re_\lambda$  decrease with streamwise distance (see table 2). It is not clear how close to the streamwise border between increasing and decreasing  $Re_\lambda$  the SFV20 station is in the  $G/H = 1.25$  wake. Table 1 shows that  $Re_\lambda$  increases from SFV7 to SFV20 in this wake and we can therefore expect SFV20 in the  $G/H = 1.25$  wake to be exceptional

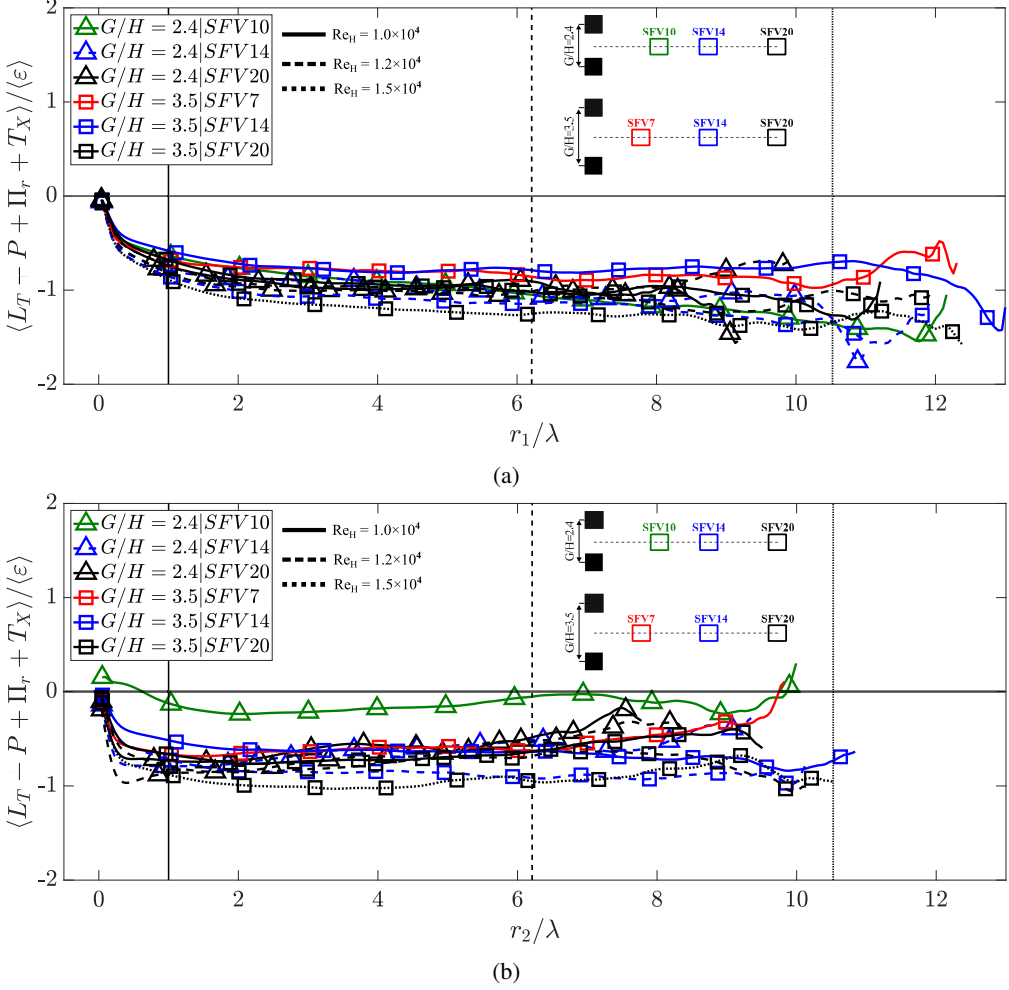


Figure 9: Normalised scale-by-scale plots of the sum of interscale and interspace transfer rates, two-point production and linear transport rates. Results are shown for separations scales in the streamwise (a) and in the cross-stream (b) directions. The vertical dashed and dotted lines represent the smallest and largest integral length scales for the SFVs, respectively.

too. Nevertheless,  $\langle T_X \rangle$  and  $\langle \Pi_r \rangle$  have opposite signs, specifically  $\langle T_X \rangle > 0$  and  $\langle \Pi_r \rangle < 0$ , and non-homogeneity is very significant down to the smallest turbulent scales (see Fig. 10) as for all the stations studied here in the other two wakes. There is no tendency towards local homogeneity at small enough turbulent length scales even at the SFV20 station of the  $G/H = 1.25$  wake where  $Re_\lambda$  nears 500.

The SFV20 station of the  $G/H = 1.25$  wake is actually unique among all the other stations studied in this paper in that  $\langle T_X \rangle^*$  grows very sharply with both  $r_1$  and  $r_2$ , in fact reaching values between 2 and 3 at  $r_1, r_2$  between  $4\lambda$  and  $6\lambda$ , see Fig. 10. The  $G/H = 1.25$  wake seems to be the one of the three wakes with recirculations reaching the furthest downstream as illustrated in Fig. 1 suggesting stronger non-homogeneity over a longer streamwise distance in multiples of  $H$ . In fact non-homogeneity is not only stronger at larger but also at the

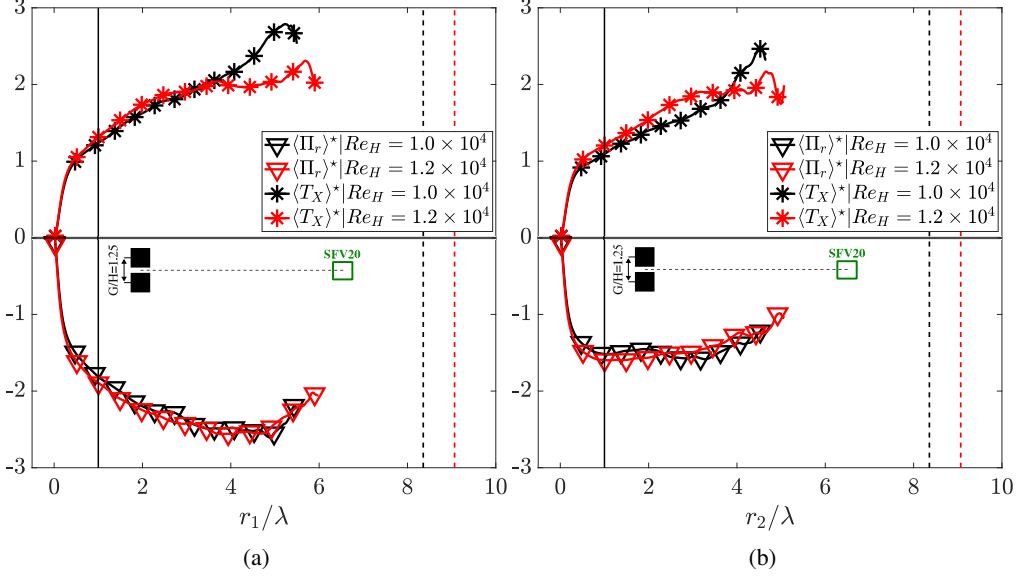


Figure 10: Normalised average scale-by-scale energy transfer rates in scale  $\langle \Pi_r \rangle^*$  and in physical  $\langle T_X \rangle^*$  space for configuration  $G/H = 1.25$  SFV20 at  $Re_H = 1.0$  and  $1.2 \times 10^4$ .

Plots are shown for separations scales in the streamwise (a) and in the cross-stream (b) direction.

smallest scales in this wake's SFV20, with  $\langle T_X \rangle^*$  between 0.6 and 0.7 at both  $r_1 = \lambda/4$  and  $r_2 = \lambda/4$ .

For  $r_2 = 0$ , the  $r_1$  profile of  $\langle \Pi_r \rangle^*$  is as sharp as the  $r_1$  profile of  $\langle T_X \rangle^*$  but opposite (see Fig. 10). Hence, similarly to all stations in the other two wakes except SFV10 for  $G/H = 2.4$  which is not quite in the decaying wake,  $\langle \Pi_r \rangle^* + \langle T_X \rangle^*$  remains about constant at  $-0.5$  over a  $r_1$  range from  $0.2\lambda$  to  $\langle \mathcal{L}_v \rangle/2$ , see Fig. 11 for  $Re_H = 1.0 \times 10^4$  ( $\langle \mathcal{L}_v \rangle/\lambda = 8.4$ ) and Fig. 12 for  $Re_H = 1.2 \times 10^4$  ( $\langle \mathcal{L}_v \rangle/\lambda = 9.1$ ). These two figures also show that the very strong non-homogeneity in  $r_1$  is limited to two-point turbulent diffusion as two-point linear transport and turbulence production are negligible compared to the other terms in the scale-by-scale horizontal two-point turbulent kinetic energy budget.

For  $r_1 = 0$ , the  $r_2$  profiles of  $\langle \Pi_r \rangle^*$  and  $\langle T_X \rangle^*$  in Fig. 10 are qualitatively closer to the exception SFV10 of  $G/H = 2.4$ : whereas  $\langle T_X \rangle^*$  increases,  $\langle \Pi_r \rangle^*$  does not decrease with  $r_2$ . In fact,  $\langle \Pi_r \rangle^*$  remains remarkably constant at about  $-1.5$  for  $r_2$  from  $\approx \lambda$  to  $\approx 4\lambda$ . Similarly to SFV10 of  $G/H = 2.4$ , Fig. 11 and Fig. 12 show that  $\langle \Pi_r \rangle^* + \langle T_X \rangle^*$  increases with  $r_2$  and that two-point linear transport and/or turbulence production are not at all negligible except at length scales below  $\lambda$  at SFV20 of  $G/H = 1.25$ . (In fact we checked that it is two-point turbulence production which is not negligible, two-point linear transport remains small in magnitude.)

We conclude from this and the previous subsections that

$$\langle \Pi_r \rangle + \langle T_X \rangle \approx -C\langle \varepsilon \rangle \quad (4.4)$$

holds for either  $r_1$  or  $r_2$  in the inertial range (bounded from below by  $\lambda$  or a fraction of  $\lambda$  and from above by an outer scale between  $\langle \mathcal{L}_v \rangle$  and  $\langle \mathcal{L}_v \rangle/2$ ), with the dimensionless constant coefficient  $C$  between 0.6 and 1.0 depending on wake and location within the wake, unless two-point production rate is not negligible (as is the case for the  $r_2$  dependencies at SFV10,  $G/H = 2.4$  and SFV20,  $G/H = 1.25$ ) or that (4.3) does not hold (as is the case for the  $r_1$

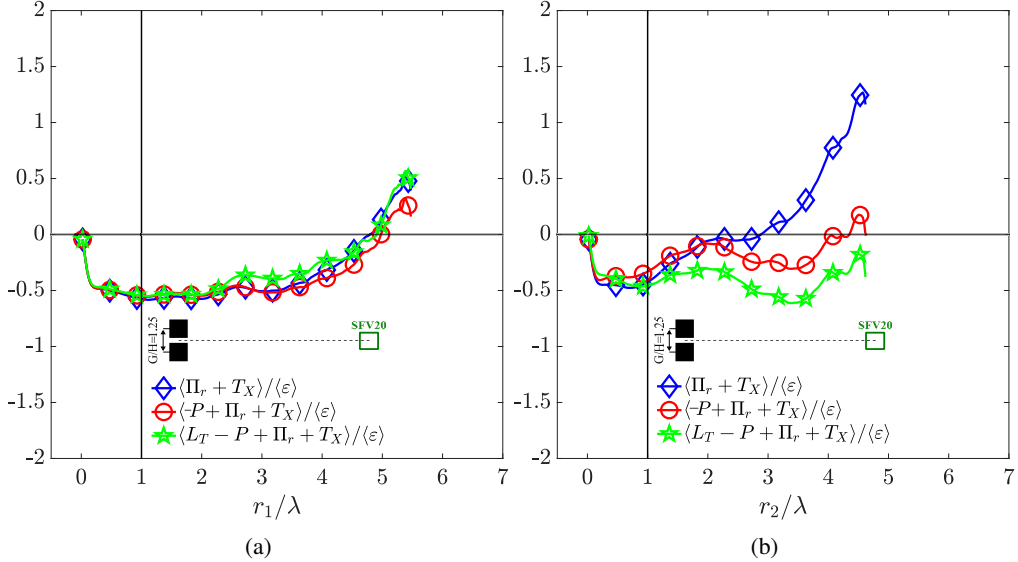


Figure 11: Normalised scale-by-scale plots of the energy transfer rate budget taking into account two-point production and linear transport for configuration  $G/H = 1.25$  SFV20 at  $Re_H = 1.0 \times 10^4$ . Plots are shown for separations scales in the streamwise (a) and in the cross-stream (b) direction.

dependence at SFV10 of the  $G/H = 2.4$  wake where two-point turbulence production rate is negligible).

Incidentally, it can be inferred from Fig. 11 and Fig. 12 that the validity of (4.3) can be very sensitive to the global Reynolds number as these figures suggest that (4.3) more or less holds versus both  $r_1$  and  $r_2$  for  $Re_H = 1.0 \times 10^4$  but not versus  $r_2$  for  $Re_H = 1.2 \times 10^4$  at SFV20 of the  $G/H = 1.25$  wake.

## 5. Concluding discussion

In all the centreline stations in the turbulence decay region or towards the downstream edge of the turbulence buildup region of all three qualitatively turbulent wakes examined here, the space-time average inter-space turbulence transfer rate is very considerable and positive down to the smallest turbulence length scales even though the local  $Re_\lambda$  reaches values of up to nearly 500. There is no tendency whatsoever towards local homogeneity, even at the smallest (viscosity affected) turbulent length scales.

In all these stations, the space-time average inter-scale turbulence transfer rate is negative and therefore has the opposite sign to the average inter-space turbulence transfer rate. Turbulence cascade and two-point turbulence diffusion act, on average, against each other at dissipative and inertial scales and even at scales above the integral scale  $\langle \mathcal{L}_v \rangle$ . In fact the average inter-scale transfer rate is comparable to and often considerably faster than the turbulence dissipation rate. Provided that the non-homogeneity is not a turbulence producing one, i.e. that two-point turbulence production rate is negligible, and that the two-point pressure-velocity term does not violate the self-similar balance (4.3), the sum of the inter-space and inter-scale turbulence transfer rates is about constant (equation (4.4)) in the inertial range of length scales. This constant is between -0.6 and -1.0 depending on wake and streamwise centreline location within the wake. The simple self-similar balance (4.4) is

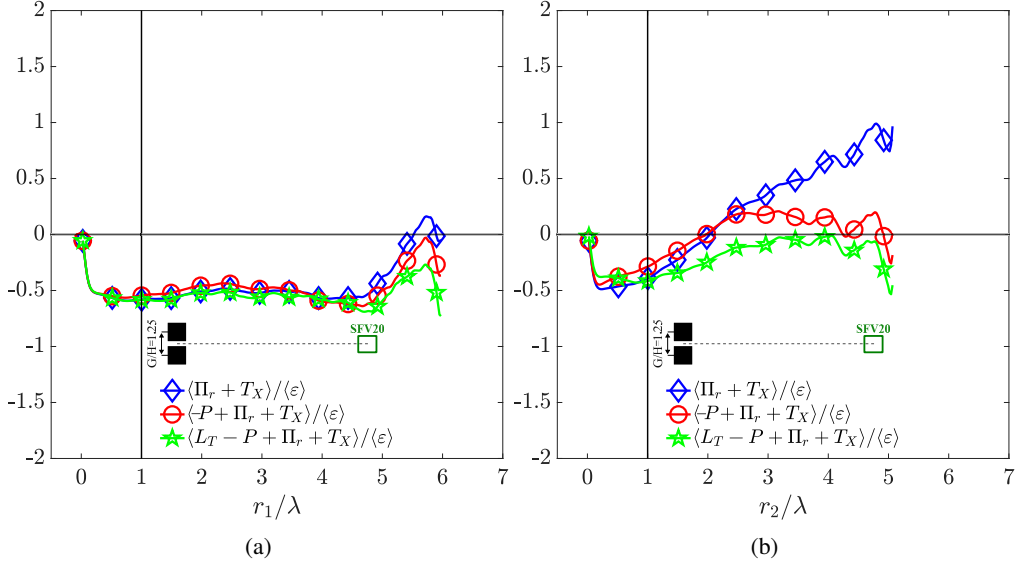


Figure 12: Normalised scale-by-scale plots of the energy transfer rate budget taking into account two-point production and linear transport for configuration  $G/H = 1.25$  SFV20 at  $Re_H = 1.2 \times 10^4$ . Plots are shown for separations scales in the streamwise (a) and in the cross-stream (b) direction.

in fact obeyed versus both  $r_1$  and  $r_2$  at any station sampled in the turbulence decay region of our turbulent wakes.

Our results for the  $G/H = 3.5$  and  $G/H = 2.4$  turbulent wakes also show that the normalised inter-scale and inter-space transfer rates  $\langle \Pi_r \rangle / \langle \varepsilon \rangle$  and  $\langle T_X \rangle / \langle \varepsilon \rangle$  are constant with a slight, perhaps linear, trend with  $r_1, r_2$  in some cases. Similar observations were made by Beaumard *et al.* (2024) under the rotating blades in a baffled water tank, who also found the same signs of  $\langle \Pi_r \rangle / \langle \varepsilon \rangle$  and  $\langle T_X \rangle / \langle \varepsilon \rangle$  as we do here. The theory of non-homogeneous turbulence of Chen & Vassilicos (2022) and Beaumard *et al.* (2024) predicts constant  $\langle \Pi_r \rangle / \langle \varepsilon \rangle$  and  $\langle T_X \rangle / \langle \varepsilon \rangle$  in the inertial range under the hypothesis of similar two-point physics at different locations of the non-homogeneous turbulence and under the assumption that two-point turbulence production is negligible. This theory therefore also predicts the self-similar balance (4.4) in the inertial range. However, the departure from constancy evidenced by the slight, perhaps linear, trend mentioned at the start of this paragraph may suggest the need of a sub-leading-order Reynolds number correction to the theory. This is one of the three open questions which now need to be addressed. The other two questions are (i) what sets the turbulence dissipation rate and (ii) what physical mechanism determines whether the inter-scale and the inter-space turbulence transfer rates cooperate or counteract each other.

Future research can begin to tackle these open questions and help test the bounds of the proposed theory by investigating off-centreline regions across a broader range of wake types and by extending the analysis to diverse types of non-homogeneous turbulent flows. For example, shearless mixing layers introduced by Gilbert (1980) and Veeravalli & Warhaft (1989) are also cases of non-producing non-homogeneity where two adjacent regions of shearless turbulence with different turbulence levels and/or length scales progressively mix. On the other hand, the layer sometimes referred to as a log-layer in turbulent channel flows and zero pressure gradient boundary layers are a case of non-transporting non-homogeneity where two-point turbulence production is present down to very small scales but average two-point inter-space transport vanishes. In the production region of a temporally evolving

turbulent jet, Cimarelli *et al.* (2021) report an intermediate range of length scales where two-point inter-space turbulence transfer and inter-scale turbulence transfer have opposite signs (see their figure 10). However, Cimarelli *et al.* (2024) find these two types of two-point transfer to have the same sign above the, so-called log-layer in wall turbulence (see their figure 7). This variability of behaviour needs to be addressed and explained perhaps in terms of a classification of turbulence non-homogeneities into a small number of universality classes each one governed by its own comprehensive theory. Ultimately, the study of turbulent diffusion–cascade interactions offers a promising entry point for advancing our understanding of the physics governing non-homogeneous and unsteady turbulent flows which are well beyond the assumptions of Kolmogorov’s equilibrium framework.

**Acknowledgements.** We are thankful to the authors of Chen *et al.* (2021) for granting us access to the data analysed in the present work. We thank C. Cuvier for the helpful discussions.

**Funding.** This work was funded by the European Union (ERC, NoStaHo, 101054117). Views and opinions expressed are, however, those of the authors only and do not necessarily reflect those of the European Union or the European Research Council. Neither the European Union nor the granting authority can be held responsible for them.

**Declaration of interests.** The authors report no conflict of interest.

**Data availability statement.** The data that support the findings of this study are available upon request.

**Author ORCIDs.** E. Fuentes-Noriega, <https://orcid.org/0000-0002-9931-7061>; J.C. Vassilicos, <https://orcid.org/0000-0003-1828-6628>

## REFERENCES

ALEXAKIS, A. 2023 How far does turbulence spread? *Journal of Fluid Mechanics* **977**, R1.

ALVES-PORTELA, F. & VASSILICOS, J.C. 2022 Inhomogeneous turbulence scalings in a free shear flow. In *Proceedings of the 12th International Symposium on Turbulence and Shear Flow Phenomena (TSFP12)*, pp. 1–6.

BEAUMARD, P., BRAGANÇA, P., CUVIER, C., STEIROS, K. & VASSILICOS, J.C. 2024 Scale-by-scale non-equilibrium with kolmogorov-like scalings in non-homogeneous stationary turbulence. *Journal of Fluid Mechanics* **984**, A35.

CHEN, J.G., CUVIER, C., FOUCAUT, J.M., OSTOVAN, Y. & VASSILICOS, J.C. 2021 A turbulence dissipation inhomogeneity scaling in the wake of two side-by-side square prisms. *Journal of Fluid Mechanics* **924**, A4.

CHEN, J.G. & VASSILICOS, J.C. 2022 Scalings of scale-by-scale turbulence energy in non-homogeneous turbulence. *Journal of Fluid Mechanics* **938**, A7.

CIMARELLI, A., ANGELIS, E. DE & CACIOLA, C.M. 2013 Paths of energy in turbulent channel flows. *Journal of Fluid Mechanics* **715**, 436–451.

CIMARELLI, A., ANGELIS, E. DE, JIMENEZ, J. & CACIOLA, C.M. 2016 Cascades and wall-normal fluxes in turbulent channel flows. *Journal of Fluid Mechanics* **796**, 417–436.

CIMARELLI, A., BOGA, G., PAVAN, A., COSTA, P. & STALIO, E. 2024 Spatially evolving cascades in wall turbulence with and without interface. *Journal of Fluid Mechanics* **987**, A4.

CIMARELLI, A., MOLLICONE, J.P., REEUWIJK, M. VAN & ANGELIS, E. DE 2021 Spatially evolving cascades in temporal planar jets. *Journal of Fluid Mechanics* **910**, A19.

FOUCAUT, J.M., GEORGE, W.K., STANISLAS, M. & CUVIER, C. 2021 Optimization of a spiv experiment for derivative moments assessment in a turbulent boundary layer. *Experiments in Fluids* **62**, 1–15.

FRISCH, U. 1995 *Turbulence: the legacy of AN Kolmogorov*. Cambridge university press.

GEORGE, W.K. & HUSSEIN, J. 1991 Locally axisymmetric turbulence. *Journal of Fluid Mechanics* **233**, 1–23.

GERMANO, M. 2012 The simplest decomposition of a turbulent field. *Physica D: Nonlinear Phenomena* **241** (3), 284–287.

GILBERT, B. 1980 Diffusion mixing in grid turbulence without mean shear. *Journal of Fluid Mechanics* **100** (2), 349–365.

HILL, R.J. 2001 Equations relating structure functions of all orders. *Journal of Fluid Mechanics* **434**, 379–388.

HILL, R.J. 2002 The approach of turbulence to the locally homogeneous asymptote as studied using exact structure-function equations. *arXiv preprint physics/0206034* .

KANEDA, Y. 2020 Linear response theory of turbulence. *Journal of Statistical Mechanics: Theory and Experiment* **2020** (3), 034006.

KOLMOGOROV, A.N 1941 Dissipation of energy in the locally isotropic turbulence. In *Dokl. Akad. Nauk. SSSR*, , vol. 32, pp. 19–21.

LAIZET, S., VASSILICOS, J.C. & CAMBON, C. 2013 Interscale energy transfer in decaying turbulence and vorticity–strain-rate dynamics in grid-generated turbulence. *Fluid Dynamics Research* **45** (6), 061408.

LARSEN, H.S. & VASSILICOS, J.C. 2023 Spatio-temporal fluctuations of interscale and interspace energy transfer dynamics in homogeneous turbulence. *Journal of Fluid Mechanics* **969**, A14.

LEFEUVRE, N., THIESSET, F., DJENIDI, L. & ANTONIA, R.A. 2014 Statistics of the turbulent kinetic energy dissipation rate and its surrogates in a square cylinder wake flow. *Physics of Fluids* **26** (9).

LUMLEY, J.L. 1992 Some comments on turbulence. *Physics of fluids A* **4** (2), 203–211.

MARATI, N., CASCIOLO, C.M. & PIVA, R. 2004 Energy cascade and spatial fluxes in wall turbulence. *Journal of Fluid Mechanics* **521**, 191–215.

THIESSET, F. & DANAILA, L. 2020 The illusion of a kolmogorov cascade. *Journal of Fluid Mechanics* **902**, F1.

VALENTE, P.C. & VASSILICOS, J.C. 2015 The energy cascade in grid-generated non-equilibrium decaying turbulence. *Physics of Fluids* **27** (4).

VEERAVALLI, S. & WARHAFT, Z. 1989 The shearless turbulence mixing layer. *Journal of Fluid Mechanics* **207**, 191–229.

## Appendix A. Scale-by-scale behaviour of $\overline{\delta K_h}$

In this Appendix we report the profiles of  $\overline{\langle \delta K_h \rangle}$  as function of the separation scales  $r_1$  and  $r_2$  normalised using the non-equilibrium scaling proposed in Chen & Vassilicos (2022). These profiles are plotted in lin-log axes in Figs. 13(a,b,c) for the  $G/H = 3.5$ ,  $G/H = 2.4$  and  $G/H = 1.25$  wakes, respectively. Unless specified otherwise, the profiles correspond to the  $Re_H = 1.0 \times 10^4$  global Reynolds. Near-identical results are obtained for the other  $Re_H$ . In Chen & Vassilicos (2022), similar plots where shown but for the longitudinal and transverse structure functions individually as a function of  $r_1$  at different  $X_2$  locations. Here, we report the behaviour of  $\overline{\delta K_h}$  averaged over SFV area as a function of both separation scale directions  $r_1$  and  $r_2$ . Same conclusions are drawn as in Chen & Vassilicos (2022). As can be seen in the lin-log plots of Figs. 13a and 13b, an approximate plateau indicating approximate 2/3 power law dependence on length-scale appears to be forming over nearly one decade between Taylor length and integral scale in the analysed SFVs for  $G_H = 3.5$  and  $G_H = 2.4$  with perhaps a slight deviation for  $G/H = 3.5$  SFV7. There is a significant departure from 2/3 power law at the SFV20 station of the  $G/H = 1.25$  wake.

## Appendix B. Inter-space energy transfer rate: dependence on averaging procedure and individual terms

### B.1. The spatial averaging dependence

The data reported in this experimental investigation was averaged over time (20 000 uncorrelated samples) and over the entire field of view (space averaging). The latter was done to yield converged third order moments, i.e converged averages of  $T_X$  and  $\Pi_r$  given that convergence of two-point statistics gradually weakens as the separation scale  $r_1$  or  $r_2$  increases. In the following, the effect of the space-average operation is assessed by replacing it with a straight line average over  $X_1$  within the field of view's bounds for a given  $X_2$  or over  $X_2$  within the field of view's bounds for a given  $X_1$ . Figures 14 and 15 show scale-by-scale plots of averaged  $T_X$  and  $\Pi_r$  normalised by  $\langle \varepsilon \rangle$  comparing the full space average (over  $X_1$

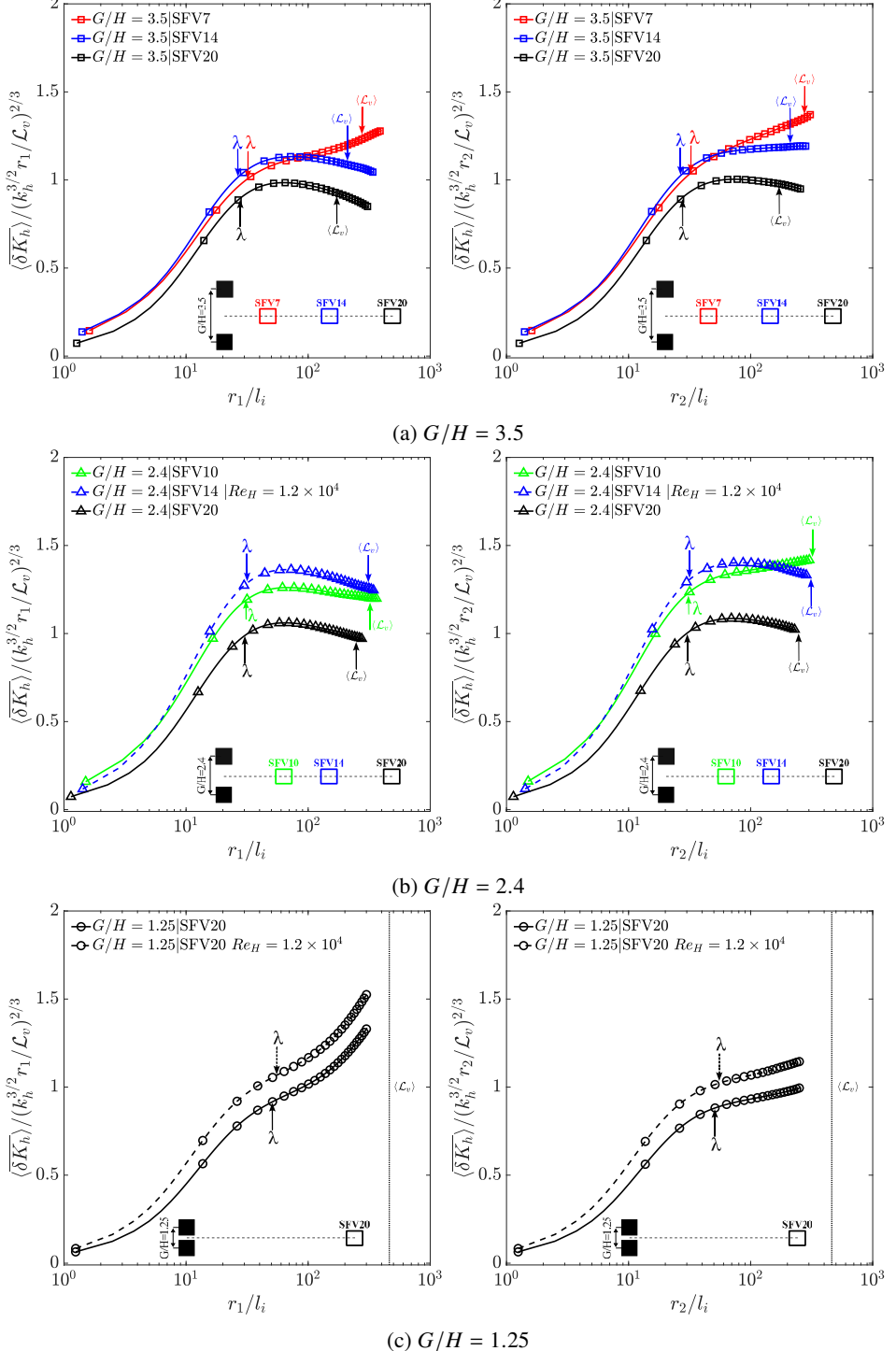


Figure 13: Normalised space-averaged two-point horizontal turbulent kinetic energy  $\langle \delta K_h \rangle$  as a function of  $r_1/l_i$  and  $r_2/l_i$ , where  $l_i = \langle \mathcal{L}_v \rangle R^{-3/4}$  with  $R = \sqrt{k_h \langle \mathcal{L}_v \rangle} / \nu$  for each wake and SFV. The Taylor length  $\lambda$  and the integral length scale  $\mathcal{L}_v$  are indicated in the plots for each SFV considered in each one of the three wakes.

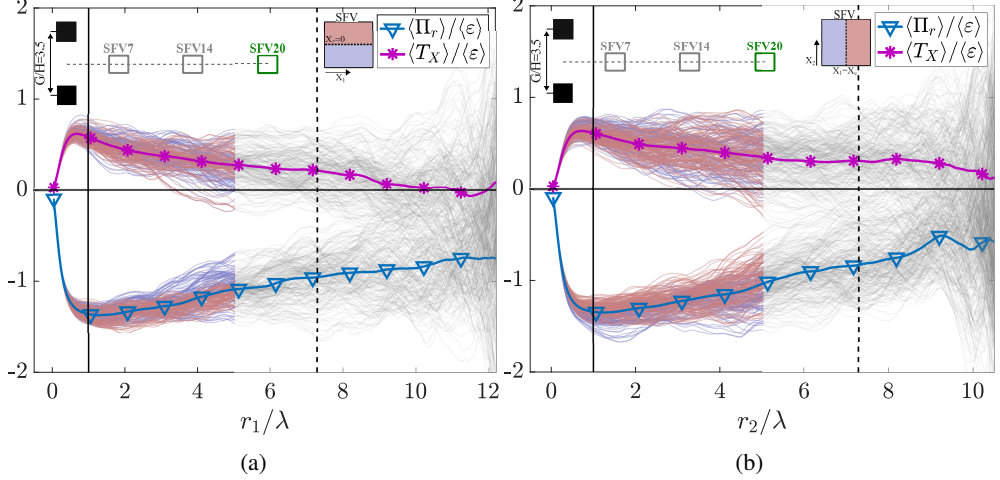


Figure 14: Analysis of the spatial averaging of inter-scale and inter-space energy transfer rates for case  $G/H = 3.5$  SFV20 at  $Re_H = 1.5 \times 10^4$ . Plots are shown for (a) quantities line averaged over  $X_1$  at a given  $X_2$  as a function of  $r_1$  and (b) quantities line averaged over  $X_2$  at a given  $X_1$  as a function of  $r_2$ . Each thin curve represents a different position in the SFV and the line averaged profiles are coloured depending on their location with respect to the center of the SFV. The thick magenta and blue lines represent the fully averaged (over  $X_1$  and  $X_2$ ) quantities. The vertical dashed line locates  $\langle \mathcal{L}_v \rangle / \lambda$ .

and  $X_2$ ) to line averaged quantities (over either  $X_1$  or  $X_2$ ) for  $G/H = 3.5$  and  $G/H = 2.4$ . Only results for the maximum available global Reynolds number and SFV20 are shown as they are representative of all other configurations. At small scales  $r_1$  or  $r_2$  where convergence is best, it is clear that the line averages of  $T_X$  do not vanish and are in fact positive for any location  $X_1$  or  $X_2$  within the SFV in both wakes. Convergence obviously weakens with increasing  $r_1$  and  $r_2$  and line-averages increasingly fluctuate as a result. Curves are blue or red if the line-average they represent is over a straight line on one or the other side of the center of the field of view. The distribution of red and blue profiles demonstrates that there is no preferential departure from the fully averaged quantities above or below the centreline or upstream versus downstream locations in the SFV. This result legitimises the use of the spatial averaging operator over the entire SFV and reinforces one of the key results of this investigation which is the absence of local homogeneity over a range of length scales reaching down to sizes as small as the Taylor length or even a fraction of it.

### B.2. Individual inter-space transfer terms

The inter-space transfer rate  $T_X$  defined in eq. (4.1) comprises two terms:

$$T_X \equiv T_{X_1} + T_{X_2} \quad (\text{B } 1)$$

where  $T_{X_1} \equiv \frac{\partial}{\partial X_1} \overline{u'_{X_1} \delta K_h}$  characterises non-homogeneity in the streamwise direction and  $T_{X_2} \equiv \frac{\partial}{\partial X_2} \overline{u'_{X_2} \delta K_h}$  characterises non-homogeneity in the cross-stream direction. In this Appendix, the individual contributions  $T_{X_1}$  and  $T_{X_2}$  are reported for all three wakes in each one of the SFV locations studied in the paper. In the same manner as the total inter-space transfer rate, each term is averaged over SFV space for converged results.

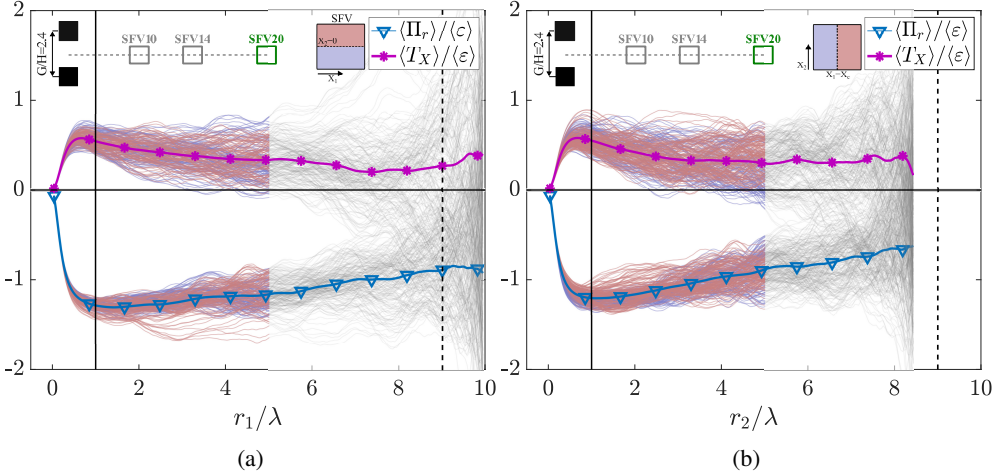


Figure 15: Analysis of the spatial averaging of inter-scale and inter-space energy transfer rates for case  $G/H = 2.4$  SFV20 at  $Re_H = 1.2 \times 10^4$ . Plots are shown for (a) quantities line averaged over  $X_1$  at a given  $X_2$  as a function of  $r_1$  and (b) quantities line averaged over  $X_2$  at a given  $X_1$  as a function of  $r_2$ . Each thin curve represents a different position in the SFV and the line averaged profiles are coloured depending on their location with respect to the center of the SFV. The thick magenta and blue lines represent the fully averaged (over  $X_1$  and  $X_2$ ) quantities. The vertical dashed line locates  $\langle \mathcal{L}_v \rangle / \lambda$ .

### B.2.1. Coupled-street $G/H = 3.5$ wake

Figures 16, 17 and 18 show scale-by-scale plots of normalised inter-space energy transfer rates  $\langle T_{X_1} \rangle^* = \langle T_{X_1} \rangle / \langle \varepsilon \rangle$  and  $\langle T_{X_2} \rangle^* = \langle T_{X_2} \rangle / \langle \varepsilon \rangle$  for  $G/H = 3.5$  at SFV20, SFV14 and SFV7, respectively. The results are shown for  $Re_H = 1.0 \times 10^4$ . It is found that, in most situations, both terms are non-zero and of same (positive) sign, indicating that both directions exhibit non-homogeneity even at small scales and that the transfer of two-point turbulent kinetic energy away from the SFV operates in both directions. For the two farthest locations SFV14 and SFV20 (Figs. 16 and 17),  $\langle T_{X_1} \rangle^*$  is generally dominant for scales  $r_1$  (with  $r_2 = 0$ ) up to around  $\langle \mathcal{L}_v \rangle$ , while  $\langle T_{X_2} \rangle^*$  is the dominant term for all sampled scales  $r_2$  (with  $r_1 = 0$ ). At SFV7, however,  $\langle T_{X_2} \rangle^*$  is dominant for both  $r_1$  and (especially)  $r_2$  (Fig. 18).

In this case,  $\langle T_{X_1} \rangle^*$  shows small negative values for  $r_2 > 5\lambda$ .

### B.2.2. Coupled street bi-stable $G/H = 2.4$ wake

Figures 19, 20 and 21 show the scale-by-scale plots of normalised inter-space energy transfer rates  $\langle T_{X_1} \rangle^* = \langle T_{X_1} \rangle / \langle \varepsilon \rangle$  and  $\langle T_{X_2} \rangle^* = \langle T_{X_2} \rangle / \langle \varepsilon \rangle$  for  $G/H = 3.5$  at SFV20, SFV14 and SFV7, respectively. Results are shown for  $Re_H = 1.0 \times 10^4$  at SFV20 and SFV10 and for  $Re_H = 1.2 \times 10^4$  at SFV14. In all cases,  $\langle T_{X_1} \rangle^*$  and  $\langle T_{X_2} \rangle^*$  exhibit the same positive sign as the total inter-space transfer rate and for all accessible scales. For the farthest location SFV20, the observations are very similar to that of  $G/H = 3.5$ . Closer to the square prisms, at SFV14 and SFV10, both  $\langle T_{X_1} \rangle^*$  and  $\langle T_{X_2} \rangle^*$  show similar magnitudes for  $r_1 > 3\lambda$  (Figs. 20 and 21). However,  $\langle T_{X_2} \rangle^*$  still dominates for all  $r_2$  scales. Once again, non-homogeneity is clearly present in both directions and such that the turbulence transfers two-point turbulent energy away from the SFV in both directions too.

### B.2.3. Close-to-single bluff body bistable $G/H = 1.25$ wake

Figure 22 shows the scale-by-scale plots of normalised inter-space energy transfer rates  $\langle T_{X_1} \rangle^* = \langle T_{X_1} \rangle / \langle \varepsilon \rangle$  and  $\langle T_{X_2} \rangle^* = \langle T_{X_2} \rangle / \langle \varepsilon \rangle$  for  $G/H = 1.25$  at SFV20 for two global

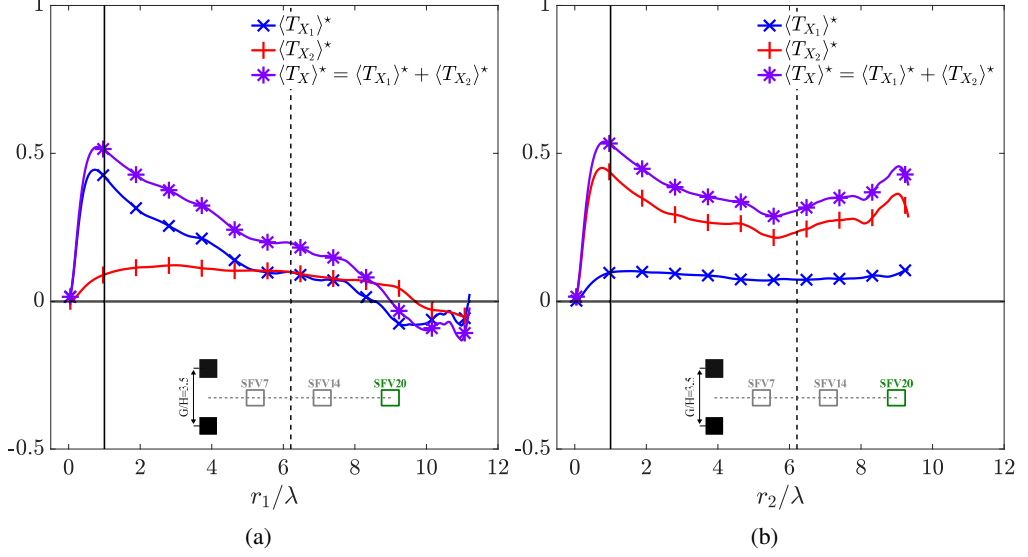


Figure 16: Normalised average scale-by-scale inter-space energy transfer rate terms  $T_{X_1}$  and  $T_{X_2}$  as a function of  $r_1$  (a) and  $r_2$  (b) for case  $G/H = 3.5$  SFV20 at  $Re_H = 1.0 \times 10^4$ . The vertical dashed line corresponds to the integral length scale location.

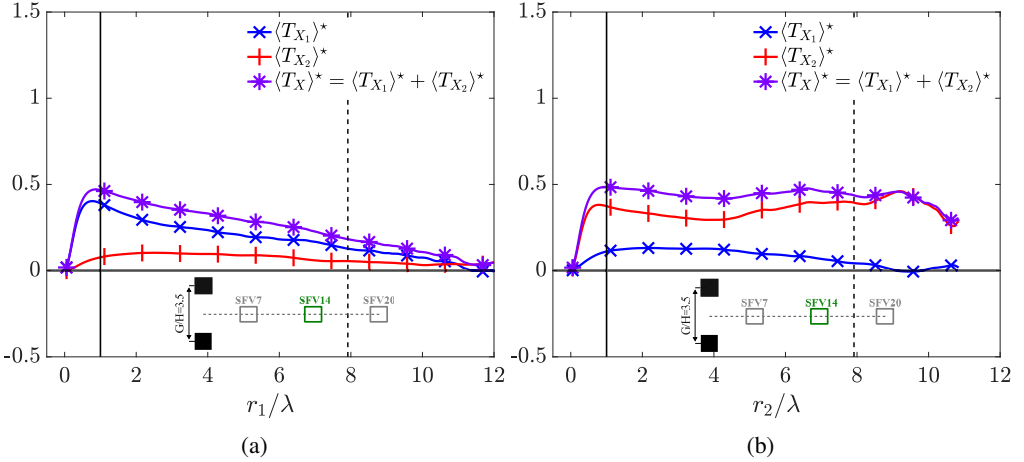


Figure 17: Normalised average scale-by-scale inter-space energy transfer rate terms  $T_{X_1}$  and  $T_{X_2}$  as a function of  $r_1$  (a) and  $r_2$  (b) for case  $G/H = 3.5$  SFV14 at  $Re_H = 1.0 \times 10^4$ . The vertical dashed line corresponds to the integral length scale location.

Reynolds number values  $Re_H = 1.0 \times 10^4$  and  $Re_H = 1.2 \times 10^4$ . As explained at the end of section 3 and in sub-section 4.4, the SFV20 location in the  $G/H = 1.25$  wake is qualitatively different from the SFV locations analysed in the other two wakes. Interestingly, it is the  $\langle T_{X_2} \rangle$  contribution to the inter-space transfer rate which dominates and grows sharply with both  $r_1$  and  $r_2$  while  $\langle T_{X_1} \rangle$  reaches a plateau beyond  $r_1 > 0.5\lambda$  and  $r_2 > \lambda$ . This indicates that the non-homogeneity is very much stronger if not mainly in the cross-stream direction in this case unlike the SFV locations we analysed in the other two wakes.

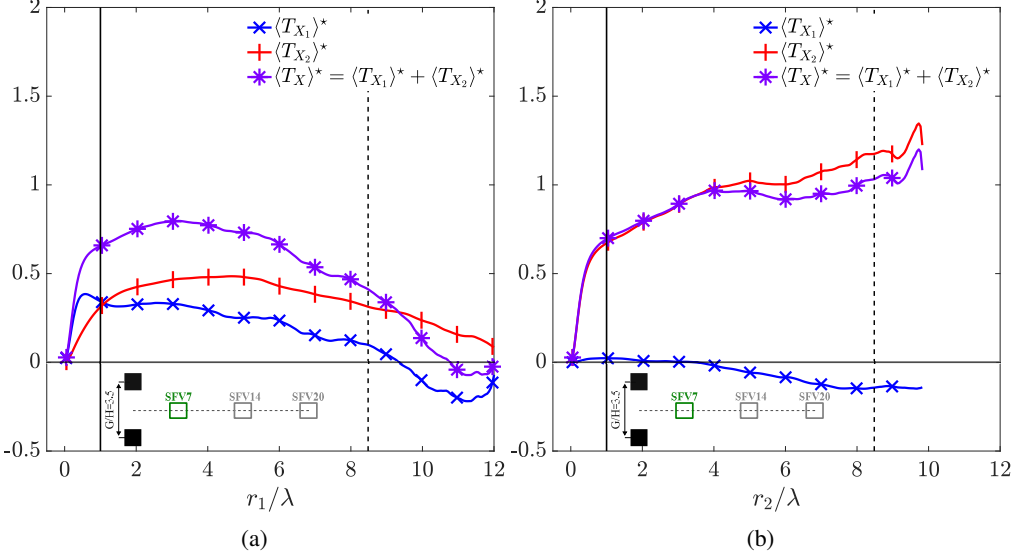


Figure 18: Normalised average scale-by-scale inter-space energy transfer rate terms  $T_{X_1}^*$  and  $T_{X_2}^*$  as a function of  $r_1$  (a) and  $r_2$  (b) for case  $G/H = 3.5$  SFV7 at  $Re_H = 1.0 \times 10^4$ . The vertical dashed line corresponds to the integral length scale location.

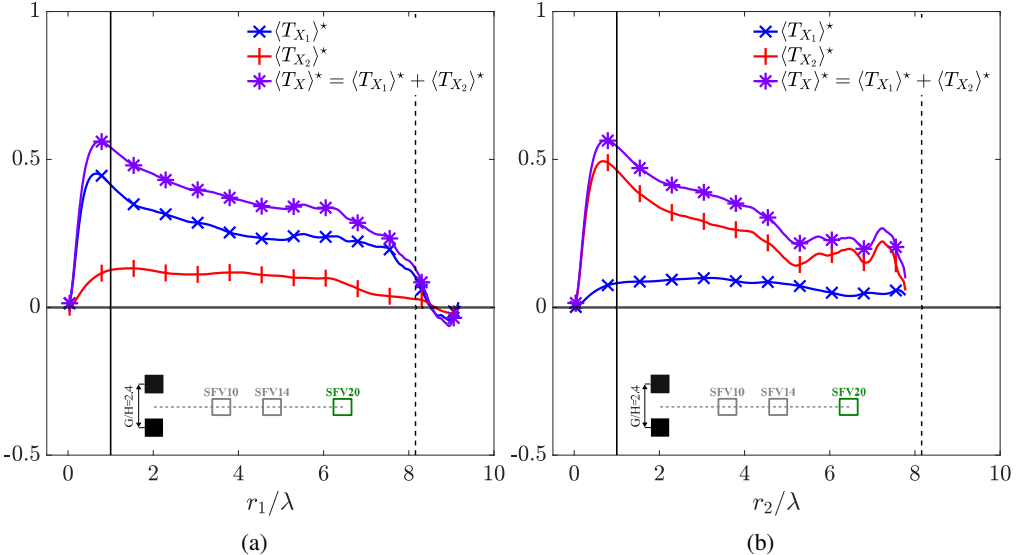


Figure 19: Normalised average scale-by-scale inter-space energy transfer rate terms  $T_{X_1}^*$  and  $T_{X_2}^*$  as a function of  $r_1$  (a) and  $r_2$  (b) for case  $G/H = 2.4$  SFV20 at  $Re_H = 1.0 \times 10^4$ . The vertical dashed line corresponds to the integral length scale location.

### Appendix C. Two-point correlation part of $\langle T_X \rangle$

Figure 23, shows the average contribution of the correlation term in the two-point inter-space transfer rate  $\langle T_X \rangle$  as described in §4 for all wakes and SFVs addressed in the present investigation. For all non-producing regions, i.e Figs. 23a-d  $Corr$  is positive and decreasing or constant in magnitude for separation scales larger than  $\lambda$ . An exception to this rule is the  $G/H = 3.5$  wake at SFV7 (Figs. 23a-b) where  $Corr$  increases with  $r_1$  and  $r_2$  from  $\lambda$  to  $3\lambda$

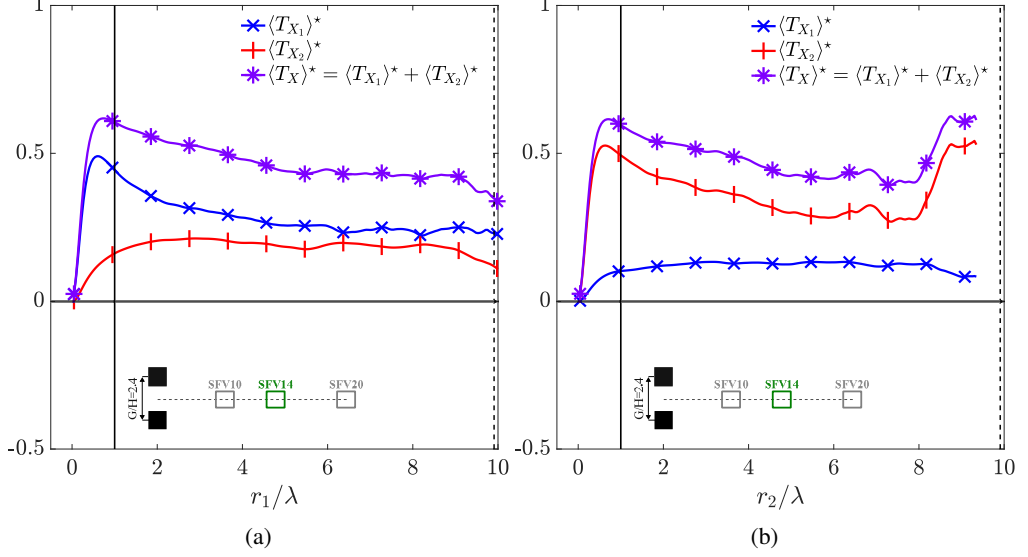


Figure 20: Normalised average scale-by-scale inter-space energy transfer rate terms  $T_{X_1}^*$  and  $T_{X_2}^*$  as a function of  $r_1$  (a) and  $r_2$  (b) for case  $G/H = 2.4$  SFV14 at  $Re_H = 1.2 \times 10^4$ . The vertical dashed line corresponds to the integral length scale location.

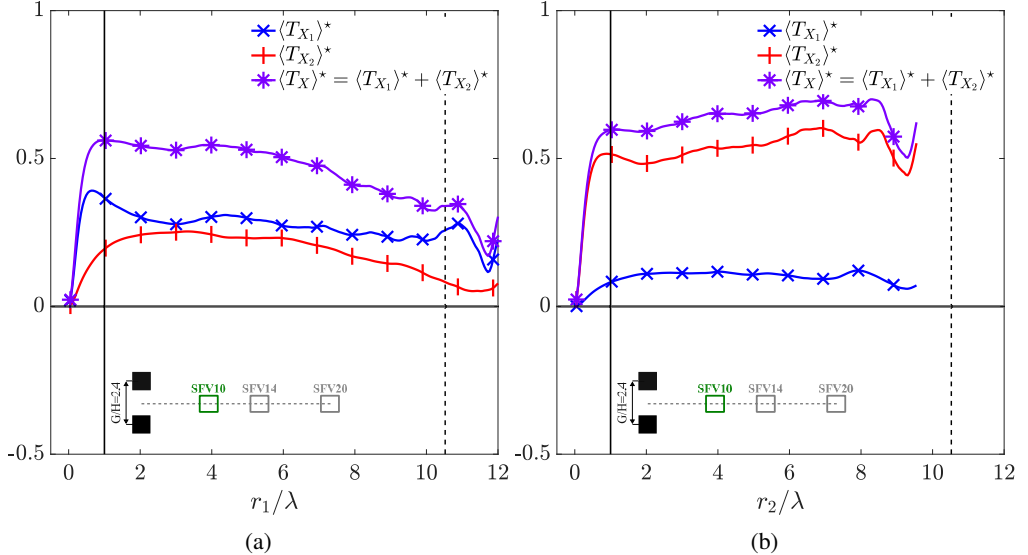


Figure 21: Normalised average scale-by-scale inter-space energy transfer rate terms  $T_{X_1}^*$  and  $T_{X_2}^*$  as a function of  $r_1$  (a) and  $r_2$  (b) for case  $G/H = 2.4$  SFV10 at  $Re_H = 1.0 \times 10^4$ . The vertical dashed line corresponds to the integral length scale location.

and  $4\lambda$  respectively but is still positive. On the other hand, as shown in Figs. 23(e-f),  $Corr$  is negative and decreasing in magnitude with increasing  $r_1$  and  $r_2$  for both values of  $Re_H$ .

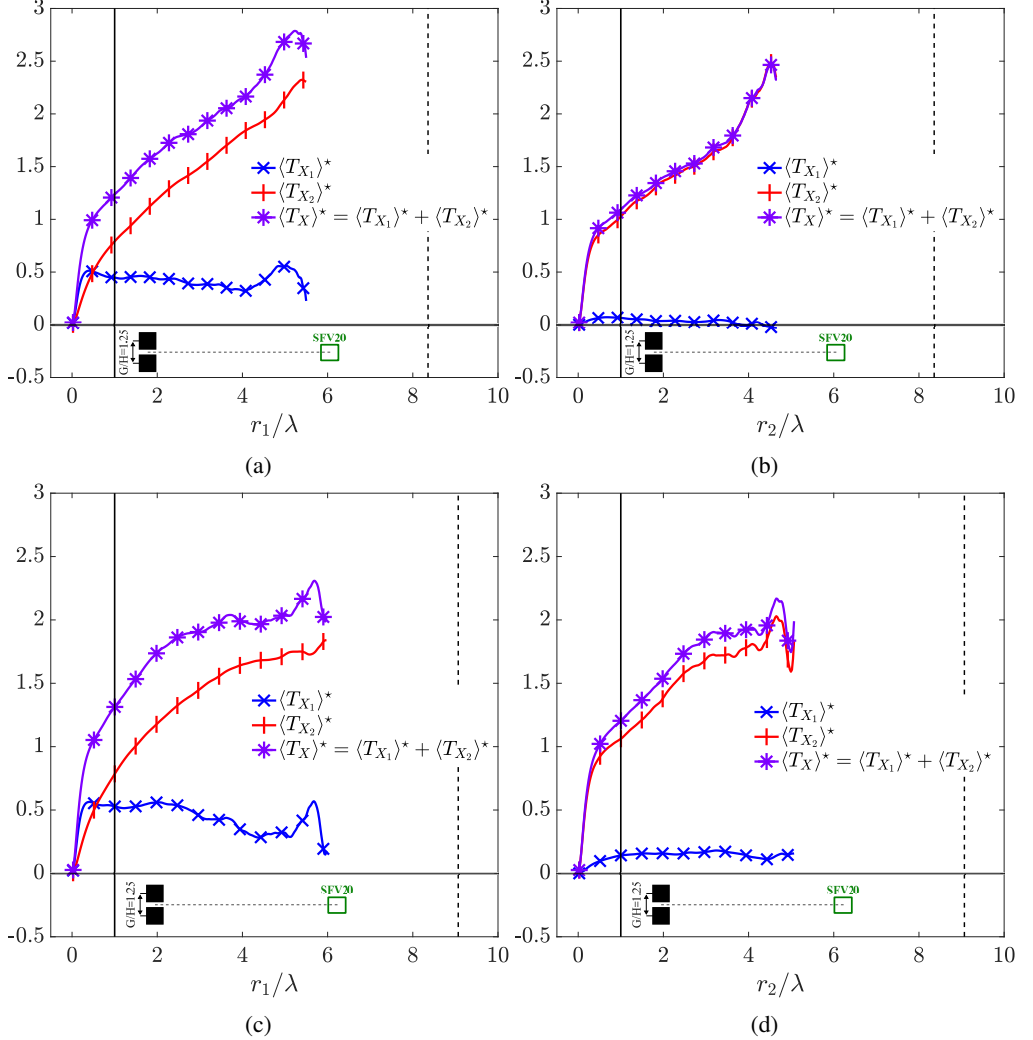


Figure 22: Normalised average scale-by-scale inter-space energy transfer rate terms  $T_{X_1}$  and  $T_{X_2}$  as a function of  $r_1$  (a) and  $r_2$  (b) for case  $G/H = 1.25$  SFV20 at  $Re_H = 1.0 \times 10^4$  and at  $Re_H = 1.2 \times 10^4$  (c) & (d). The vertical dashed line corresponds to the integral length scale location.

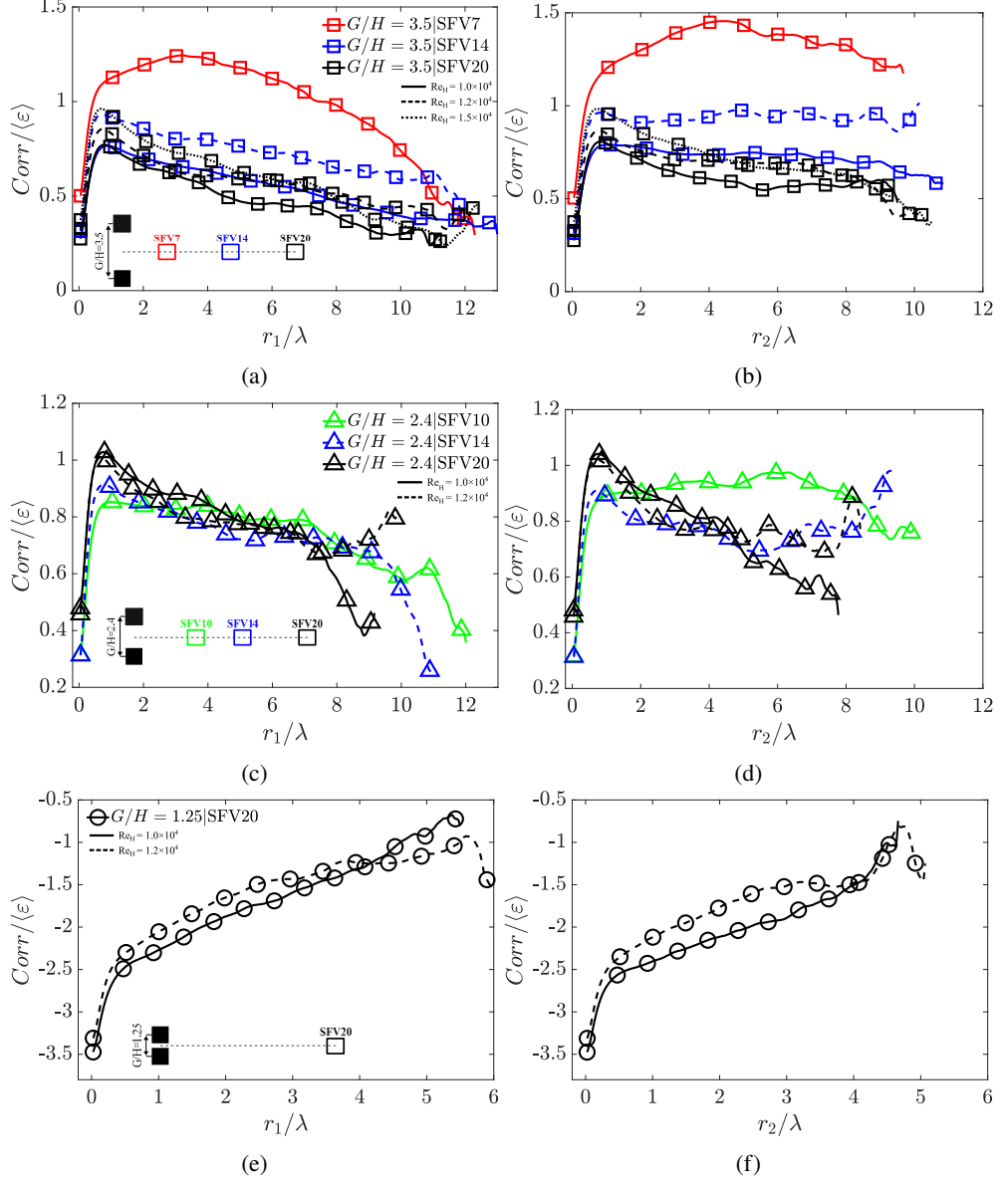


Figure 23: Average two-point correlation contribution to the inter-space transport term  $Corr = \langle T_X \rangle - \langle \mathcal{T}^+ \rangle - \langle \mathcal{T}^- \rangle$  normalised by  $\langle \varepsilon \rangle$  for (a-b)  $G/H = 3.5$ , (c-d)  $G/H = 2.4$  and (e-f)  $G/H = 1.25$  in the addressed SFVs and for all available  $Re_H$ .